Intraseasonal Oscillations over South America: A Study with a Regional Climate Model

Baode Chen[1*] and Winston C. Chao[2]

[1]GEST Center, University of Maryland, Baltimore County, Baltimore, MD, USA

[2]NASA/Goddard Flight Center, Greenbelt, MD, USA

February 2004

(Submitted to J. of Climate)

[*]*Corresponding author address:* Dr. Baode Chen, GEST, Mail Code 913, NASA/Goddard Space Flight Center, Greenbelt, MD 20771, E-mail: Baode.Chen.1@gsfc.nasa.gov

Abstract

The National Center for Atmospheric Research (NCAR) regional climate model version 2 (RegCM2) is used to investigate the observed characteristics of intraseasonal oscillations over South America. Our study is mainly concentrated on an intraseaonal mode, which is observed to account for a large portion of the intraseasonal variation, to have a standing feature and to be independent of the MJO. The NCEP/DOE AMIP-II reanalysis is utilized to provide initial and lateral boundary.

Our results indicate that the intraseasonal oscillation still exists with time-averaged lateral boundary condition, which prevents the MJO and other outside disturbances from entering the model's domain, suggesting a locally forced oscillation responsible for the intraseasonal mode independent of the MJO. Further experiments show that the annual and daily variabilities and a radiative-convective interaction are not essential to the locally forced intraseasonal oscillation. The intraseasonal oscillations over Amazon in our model essentially result from interactions among atmospheric continental-scale circulation, surface radiation, surface sensible and latent heat fluxes, and cumulus convection. The wavelet analyses of various surface energy fluxes and surface energy budget also verify that the primary cause of intraseasonal oscillation is the interaction of the land surface processes with the atmosphere.

1. Introduction

Since its discovery in 1971, the Madden-Julian Oscillation (MJO) has been intensively studied in observational data investigations, model simulations and theoretical analyses. These studies have led to many findings of the characteristics of the MJO and better understanding of the observed MJO properties as well. The MJO convection originates from the western Indian Ocean, propagates eastward, enhances over the maritime continent, and weakens and dissipates in mid-Pacific. The MJO signal in circulation fields, such as upper zonal wind, propagates around the globe with a predominant wave-number one and two pattern (e.g. Madden and Julian 1994). Theoretical work, coupled with modeling investigations, pointed out that the interaction between large-scale motion and convection in the atmosphere, together with surface fluxes could be the basic mechanism responsible for the oscillation and propagation (e.g. Hayashi and Golder 1993; Chao and Deng 1998). However, the detailed mechanism is still unknown. In the past, the studies of intraseasonal oscillation have focused on the Indian Ocean and western Pacific; but gradually, the domain of interest has been extended. The region of South America has started to gain some attention.

A regular and pronounced annual cycle in rainfall features the climate of South America. Austral summer (DJF) is the rainy season, and austral winter (JJA) is the dry season. From JJA to DJF the rainfall season starts progressively from the northwestern parts to central and southeastern Brazil, following the annual migration of the deep tropical convection and the establishment of a heat low in central South America in summer. The background summer circulation regime over South America is the South American summer monsoon (SASM), which is induced by strong adiabatic heating over

the subtropical South American highland centered at the Altiplano Plateau (Zhou and Lau 1998). The seasonally varying low-level wind, which is superimposed on the annual mean trades, between the western Sahara and Gran Chaco shows a clear reversal of its direction from winter to summer season. In their SASM study, Zhou and Lau (1998) documented a coherent 30-60 day oscillation of monsoon activities during 1989/90 austral summer season. Liebmann et al. (1999) found a 40-50 day oscillation in OLR (outgoing longwave radiation) over tropical South America. Using the singular spectrum analysis (SSA) technique, Paegle et al. (2000) demonstrated that a dipole convection pattern, with centers of action over the South Atlantic convergence zone (SACZ) and the subtropical plains, is modulated by modes with periods of 30-40 days and 22-28 days. In these studies, the intraseasonal oscillations over South America were attributed to the influence of MJO propagating into the domain. Recently, Zhou and Lau (2002) pointed out that, in addition to the two leading modes, which are in a close relationship with the MJO, there exists a third mode accounting for a large portion of the intraseasonal variation in South America. This component is a standing oscillation and is independent of the MJO. They suggested that a local forcing mechanism is responsible for this independent intraseasonal mode. This mode is the focus of this paper.

As proposed by Hu and Randall (1994 and 1995), a stationary or quasi-stationary component in the intraseasonal oscillations can be produced by nonlinear interaction among radiation, cumulus convection, and surface fluxes of sensible heat and moisture. A quasi radiative-convective equilibrium is essential to maintain the oscillation and feedback of large-scale motion on the latent heating is not required. In addition, their numerical experiments show that the oscillations are favored by warm sea surface

temperature and weak surface wind speeds. Despite that Amazon is the most distinct tropical convection center in the western hemisphere and the fluxes from its surface of tropical rainforests are close to those from the warm tropical ocean, Hu and Randall's theory can not be directly used to interpret the oscillations, because land-atmosphere interaction and land surface hydrological cycle, which play key roles in forcing and maintaining convective storms locally (as will be explained lately), are not considered in their work. Unlike sea surface temperature, ground temperature is much more sensitive to variation of the solar radiation, most convective storms are mainly forced and maintained locally due to conditional instability in the vertical distribution of atmospheric temperature, which is closely associated with surface wet-bulb temperature (Elfatih et al, 1996). Moreover, Hu and Randall did not claim that their interpretation could be used for South America. In the present study, we narrow down the likely causes for the observed characteristics of the standing component of the intraseasonal oscillations over South America, which is based on the simulation results using the National Center for Atmosphere Research (NCAR)'s Regional Climate Model version 2 (RegCM2).

A regional model has some advantages in studying this specific subject. As general circulation models (GCMs), regional climate models attempt to simulate the regional atmospheric phenomena as realistically as possible and, as a result, they include as many physical mechanisms as reasonably possible. Any associations with the rest of globe are controlled by the regional model's boundary conditions provided by either observed data or GCM's output. This characteristic allows experiments that would be impossible to do using GCMs. For example, with a regional model, the boundary condition can be filtered to remove any signals related to external MJO (i.e., MJO outside

of the model domain), preventing any MJO from propagating into the region considered. Using a regional model we can see if the intraseasonal oscillation can develop in the model domain without forcings from outside. Another advantage of a regional model is the potential increase in resolution. A higher resolution could be implemented when only modeling a relatively small region. Moreover, when compared with those of the GCMs, the simulated fields produced by the regional model with the one-way nesting system have provided a better representation of the South American climate (e.g., Nicolini et al. 2002) as the result of higher resolution.

The considerations mentioned above have provided the motivation for this work. In this paper, we have carried out a series of numerical experiments to study the standing component of the intraseasonal oscillations over South America. In Section 2, we describe the data and methodology including the model used and experimental design. The simulated results and their comparison are presented in Section 3. Section 4 discusses the physical mechanisms behind the oscillations. Finally, the conclusion and discussion are given in Section 5.

2. Data and Methodology

a. Model description

The NCAR regional climate model version 2 (RegCM2) is used. A detail description of the RegCM2 can be found in Giorgi et al. (1993a, b) and Giorgi and Mearns (1999). Here only a brief summary of the main features is provided.

The dynamical component of the RegCM2 is essentially the same as that of the MM4 (The NCAR-Pennsylvania State University Meso-scale Model version 4), which is a compressible, grid-point model with hydrostatic balance and vertical σ-coordinate. Exceptions are the use of a split-explicit time integration scheme and of an algorithm for reducing horizontal diffusion in the presence of steep topographical gradients (Giorgi et al. 1993a, Giorgi et al. 1993b). A number of physics parameterization schemes have been adopted in the model for applications to climate studies. The radiative transfer package is that of the NCAR Community Climate Model version 3 (CCM3), and the boundary layer scheme from Holtslag et al. (1990). The latest version of BATS 1E (Biosphere-Atmosphere Transfer Scheme) (Dickinson et al. 1992) was incorporated into the model to perform the surface physics calculations. The mass flux scheme of Grell et al. (1994) was implemented for cumulus convection parameterization. The subgrid explicit moisture scheme of Pal et al. (2000) was employed to calculate large-scale cloud and precipitation.

b. Data

In this study, observational data are used to force the RegCM2 and to determine the quality of the model output. The National Centers for Environmental Prediction (NCEP)/ Department of Energy (DOE) Atmospheric Model Inter-comparison (AMIP-II) reanalysis is utilized to provide initial and lateral boundary conditions for the RegCM2 based upon the 00Z, 06Z, 12Z and 18Z data. The NCEP/DOE AMIP-II reanalysis (R-2) is an updated version of the widely used NCEP/NCAR Reanalysis (R-1), which covers 1979-present, and it features newer physics and observed soil moisture forcing and also eliminates several previous errors (Kanamitsu et al., 2002). The sea surface temperature

(SST) is taken from the extended reconstructed SST data of NOAA/National Climatic Data Center (NCDC), which were constructed using the most recently available Comprehensive Ocean-Atmosphere Data Set (COADS) SST data and improved statistical methods that allow stable reconstruction using sparse data (Smith and Reynolds 2003). In addition, CMAP (Climate Prediction Center Merged Analysis of Precipitation) precipitation data (Xie and Arkin 1996) are used to evaluate the quality of the simulations.

c. Experimental design

The model domain and topographical field selected for the simulations are illustrated in Figure 1, which includes the whole continent of South America and extends farther east and west to cover a relatively large portion of both eastern Pacific and western Atlantic oceans. The model grid point spacing is 80 km and the domain size is 110 x 120 grid points. The model has 14 vertical levels with a tropospheric resolution of about $\sigma = 0.1$ and the top at 80 hPa. The period of simulation is the 607 days from September 1, 1996 to March 31, 1998 and the data of the last 516 days are used to perform analysis, i.e., the first 91 days are dropped to allow for model's spin-up. The choice of integration period was based on the consideration of that 1997 was a relatively "normal" year devoid of any active El Nino or La Nino event.

The strategy of the experiments is as follows. First, we conducted a simulation using the parameter setting described in section 2a and the lateral and surface boundary conditions are supplied at a 6-h interval from the NCEP R-2 and SST data. This simulation is referred to as the Control (CNTRL) experiment. Then, a series of

sensitivity experiments is designed and carried out: (1) experiment CBC, in which the lateral boundary conditions and sea surface temperature are the temporal means of those of CNTRL. In this experiment, the disturbances from outside of model domain are eliminated, and any temporal variation is the result of the model internal physical processes and relevant local forcing. (2) experiment CRD, the same as CBC but the longwave and shortwave heat rates of the atmosphere are specified as the temporal and spatial means of CNTRL (i.e. only functions of height) but the radiation components used in the surface energy budget were calculated from the full radiation package. This setting prevents convective-radiative interaction in the atmosphere. (3) experiment NZEN, the same as CRD, but the zenith angle was set to a constant which eliminates annual and daily variation in the surface radiation calculations. The setting prevents annual and daily cycles operating in the model. (4) experiment NDIA, the same as NZEN but it allows the annual cycle (but not the diurnal cycle) in the surface radiation. (5) experiment NANU, the same as NZEN but it allows the diurnal cycle (but not the annual cycle) in the surface radiation. (6) experiment WSFC, the same as NZEN but all grid points in the domain are defined as water surface with fixed SST which is set to the time mean of surface temperature from CNTRL run, thus all external forcings do not vary with time, and there are no interactions between atmosphere and external forcings. Table 1 summaries the experiments performed.

d. Statistical Methodology

To detect and reconstruct intraseasonal signals from the simulations, the Singular Spectral Analysis (SSA) is used in the study. The SSA is a statistical technique related to EOF analysis but is in the time domain (Ghil et al. 2001). Given a time series x_i with length N, its lagged autocorrelation matrix $\mathbf{C}$ up to lag M can be obtained, where M is

called window length, and the eigenvalues e_k of matrix **C** can be calculated through the eigenvector decomposition. The square roots of e_k are the singular values and the eigenfunctions are the EOFs in the time domain (T-EOFs). Periodic and quasi-periodic oscillations appear as paired eigenvalues and associated T-EOFs are in quadrature with each other. Two natural criteria based on the spectral properties of the eigenvector are used to select the eigenvalue pairs. In addition, the original time series can be projected onto the selected T-EOFs to obtain a reconstructed time series which represents the essential part of the oscillations. Since the SSA modes are not purely sinusoidal, the dominant periods are estimated through the Maximum-Entropy Spectral Estimates (MEM) from the reconstructed time series. An advantage of SSA over other spectral technique is that, due to its data-adaptive basis function, it can capture anharmonic oscillations, of possible nonlinear origin, by a single pair of T-EOFs, rather than by multiple spectral peaks.

Before applying SSA to a time series, the trend in the data is removed by using a time series decomposition approach STL, developed by Cleveland et al. (1990). STL is a Seasonal-Trend decomposition procedure built based on the LOESS. LOESS is the LOcally wEighted regreSion Smooth method. Unlike other trend decomposition methods with pre-specified basis functions (such as harmonic analysis), STL is essentially a data-adaptive approach and ensures that the robust estimate of trend is not distorted by aberrant behavior of basis functions and time series.

3. Model results and comparison

a. Control experiment

We begin our analysis with the results from the CNTRL run (see section 2c). Fig.2 shows December – March mean precipitation comparing with that of CMAP precipitation. The RegCM2-simulated rainfall appears to be deficient, in particularly, in the regions near the boundaries. However, the model captures the rainfall maxima in Amazon and the SACZ where the most active intraseasonal oscillations locate, furthermore, the model also simulates the dry conditions in the southeastern region. Previous studies (Fu et al 2001 and Seth et al 2003) indicated that the Amazon rainfall may be more sensitive to local forcing. Given our purpose to investigate a presumably locally forced intraseasonal oscillation and the capability of current regional climate models, the simulation is fairly sufficient. In the present paper, we will mainly concentrate on the Amazon region, which is outlined in Fig.1 and Fig.2.

Fig.3a shows time series of the mean rainfall in the Amazon region along with seasonal trend detected by using the STL approach. It can be seen that a strong seasonality exists in the simulated precipitation with maxima in the austral summers and a minimum in the austral winter. The amplitude of seasonal cycle is about 2.5 mm/day. Fluctuations with time-scales less than seasonal variation can be found to be superposed on the seasonal cycle, and are shown as the time series of precipitation anomaly in Fig. 3b by a thin line. To detect periodic oscillations, SSA is applied to the time series of anomaly in Fig. 3b. The singular spectrum is obtained as displayed in Fig. 3c. Based on significance test (same frequency and strong FFT criteria), the spectrum has three pairs of oscillatory modes, PC-1 and PC-2, PC-3 and PC-4, PC-5 and PC-6. Using these oscillatory modes, a reconstructed time series (or pre-filtered time series) can be obtained and is illustrated in Fig 3b by a thick line. To estimate the period, MEM spectrum

analysis is performed on reconstructed time series and the result is shown in Fig 3d. A clear peak at 34.8 days (0.0287 cycles/day) exists indicating there is an evident intraseasonal oscillation in the Amazon region.

b. Experiment CBC

To isolate the effects of the model internal physical process and relevant local forcing, the model was integrated with temporal mean lateral and surface boundary condition. Figs. 4a-b show time series of precipitation averaged over the Amazon region and MEM spectrum of the reconstructed time series based SSA. The precipitation in CBC displays a clear seasonal cycle superposed by fluctuations with shorter time-scale (Fig.4a). In comparison with CNTRL, the short time-scale fluctuations have rather smaller amplitudes. Unlike that of CNTRL, the peak of spectrum associated with intraseasonal time-scale in Fig. 4b is not sharply defined and is less well separated. As shown in the plot, intraseasonal oscillations tend to have two peaks, roughly, one with 47 days and other with 33 days. This suggests that internal dynamics of atmosphere and localized forcing could excite intraseasonal oscillation modes without the MJO propagating into the model domain from outside. In addition, the regression of filtered precipitation against 200 hPa winds (figures not shown) shows a Gill-type-like pattern indicating a feature of the response to thermal forcing.

c. Experiment CRD

Hu and Randal's theory (1994) emphasizes the importance of a quasi radiative-convective equilibrium to maintain stationary or quasi-stationary component in intraseasonal oscillation over sea surface. To examine whether Hu and Randal's theory is still applicable to explain the intraseasonal oscillation in our simulations, CRD was

carried out, in which convective-radiative interaction is eliminated in the atmosphere (see Section 2c). The time series of precipitation averaged over the Amazon region of CRD and MEM spectrum of the reconstructed time series based SSA are illustrated in Fig.5a – 5b. Compared with those of CNTRL and CBC, the mean precipitation of CRD is approximately 1mm/day higher, which is believed to result from more radiative energy absorbed by the surface due to lack of the interaction between convection and radiation. As apparent from Fig. 5b, a well-defined spectral peak is found within intraseasonal frequency range around 34 days. In CRD, besides the coupling between convection and atmospheric circulation, there is only one response-feedback process, i.e., the interaction between land surface and atmosphere. Therefore, these results suggest that, without a quasi convective-radiative equilibrium in which convection and radiation are closely coupled and interactive, the interaction between land surface and atmosphere along with the atmospheric dynamics is responsible for intraseasonal modes seen in Amazon.

d. Experiments NZEN, NDIA, and NANU

As shown above, the interaction between land surface and atmosphere is the most essential factor responsible for intraseasonal oscillations in Amazon. Not only does this interaction lead to a surface energy balance, but it also adjusts the atmosphere to a new structure compatible with the energetic constraints through the dynamics and thermodynamics operating within the atmosphere. The annual and diurnal cycles are the most primary time-scales in the physical processes of the model. In order to acertain whether annual and diurnal variations have significant effect on the oscillations, NZEN (both annual and diurnal cycles turned off in the radiation calculation), experiments NDIA (diurnal cycle turned off), and NANU (annual cycle turned off) are conducted.

Fig. 6a presents the MEM spectrum of SSA reconstructed time series of the precipitation from NZEN. Three separated peaks can be found at about 33.3 days, 24.4 days and 20 days. Fig. 6b shows the MEM spectrum for NDIA run. It can be seen that, without diurnal cycle, intraseasonal oscillation still exists with two peaks at roughly 33.4 days and 23.8 days. MEM spectrum for NANU is illustrated in Fig. 6c. Like NZEN and NDIA, the most significant oscillation in NANU is within intraseasonal range at 22.3 days, although a relatively high frequency. In both experiments, NZEN, NANU, the solar declination angle is that of Jan. 15th. Therefore, these three experiments suggest that annual and diurnal cycles have no decisive effects on the oscillations. These results are consistent with Hu and Randall (1994)'s study. These three experiments are carried out in a way that the time mean incident solar radiation is the same as the mean value of that of the control run. However experiments with larger incident solar radiation, for example hour angle fixed at local 12 pm., produce oscillations with higher frequency than intraseasonal time-scale (not shown).

e. Experiment WSUF

WSUF is the same as NZEN but all grids are set to water surface, therefore the interaction between land surface and atmosphere is turned off in the model. Fig. 7 shows time series of precipitation average over the model domain of this experiment. Not surprisingly, there are no significant oscillations found by using SSA, and the WSUF experiment only produces irregular fluctuations with no clear spectral peaks.

On the basis of our results, we conclude that the standing intraseasonal oscillations over Amazon in our model essentially result from interactions among atmospheric

dynamics, surface radiation, the surface sensible and latent heat fluxes, and cumulus convection. Thus in the next section we will analyze surface energy fluxes and their relationship with precipitation in the intraseasonal time-scales to explore the nature of the oscillation. We will concentrate on the results of CRD experiment, which is considered to be the most representative.

4. Interaction between surface processes and atmosphere revealed from the surface energy exchange

The incoming solar energy is stored by the oceans and continents, and eventually returns to the atmosphere. Over land, the delay between change in absorbing radiative energy and change in net energy returning to the atmosphere is much shorter than that over oceans. This is because of the much smaller heat capacity over land than over oceans. Our numerical experiments demonstrate that the interaction between surface processes and the atmosphere leads to the intraseasonal oscillation over Amazon. Because of a very short time delay of energy exchange, or, in other words, almost immediate mutual response between the surface and the atmosphere, the various surface energy fluxes in the surface energy exchange, which is governed by the surface energy budget equation, should also exhibit oscillations with the intraseasonal time scale. In order to demonstrate the roles of various surface energy exchanges as well as to verify our conclusion, an analysis of the surface energy balance has been carried out.

The land surface energy budget equation can be written as

$$C\frac{\partial T_g}{\partial t} = S_g + F_{IR}^{\downarrow} - F_{IR}^{\uparrow} - SHF - LHF - S_m$$

where C is the total heat capacity of the ground, T_g is ground temperature, S_g is surface absorbed solar flux, $F_{IR}^{\downarrow}$ is downward long-wave radiation flux reaching surface, $F_{IR}^{\uparrow}$ is infrared radiation flux emitted from the ground, SHF and LHF represent atmospheric sensible and latent heat fluxes from the ground to the atmosphere respectively, and S_m is the energy flux associated with other processes such as snow melt in the presence of snow.

The processes associated with energy exchanges between the land surface and the atmosphere are highly nonlinear, it is natural and reasonable to expect that periodic oscillations in various energy fluxes, if existing, could show an intermittent or localized characteristics within a time series. Wavelet analysis is a common tool to for analyzing localized variance of power. In order to identify the intraseasonal oscillations, wavelet analysis (e.g., Torrence and Compo 1998) is applied to the Amazon region averaged time series of T_g, S_g, $F_{IR}^{\downarrow}$, $F_{IR}^{\uparrow}$, SHF and LHF from the CRD experiment.

Figure. 8 shows the normalized local wavelet power spectrum of the precipitation using the Morlet wavelet. The normalization of the power spectrum was made by $1/\sigma^2$, where σ^2 is the variance of a white-noise time series. Thus the normalization gives a measure of the power relative to white noise. The cross-hatched region is the cone of influence, where zero padding has reduced the variance. In Fig. 8, the predominant feature is the power concentrated within the intraseasonal band around 30-day, although

the intermittence or localization of the oscillation is evident. The strongest intraseasonal oscillation can be seen during the period between day 280 and day 420. In addition, appreciable power at a longer period and synoptic time-scale is also found. Figures 9a – 9f illustrate the wavelet power of T_g, S_g, $F_{IR}^{\downarrow}$, $F_{IR}^{\uparrow}$, *SHF* and *LHF* along with their time series from the CRD experiment, respectively. From Figs. 9a – f, the most marked intraseasonal oscillations are shown from day 280 to day 420 in the power spectra of T_g, S_g, $F_{IR}^{\downarrow}$, $F_{IR}^{\uparrow}$, and *SHF*, but the strongest intraseasonal oscillation in the *LHF* occurred after day 400. In general, the most distinct intraseasonal variability exists during almost the same period for all surface fluxes and precipitation. Therefore, the results from wavelet analysis further demonstrate that the land-atmosphere interaction plays a key role in the excitation and maintenance of the standing component of intraseasonal variability in South America.

To provide an example of the surface energy budget in the intraseasonal time-scale, the time series of the precipitation, T_g, S_g, $F_{IR}^{\downarrow}$, $F_{IR}^{\uparrow}$, *SHF* and *LHF*, subject to a band filter of 30-50 days, are plotted between day 320 and 380 in Figure 10. During a positive phase of the precipitation, i.e., enhanced precipitation, for instance, the period of day 310 to 340, T_g shows a slight decrease. Both S_g and *SHF* are reduced, and the amounts of reduction are comparable. It is believed that the reductions of S_g and *SHF* are due to increased clouds and decreased surface temperature. With decreased T_g, $F_{IR}^{\uparrow}$ dwindles, but *LHF* enlarges under a surface condition with lower T_g and enhanced surface moisture due to intensified precipitation. Moreover $F_{IR}^{\downarrow}$ shows a phase lead

relative to the precipitation by about π/2 suggesting a phase difference between temporal evolutions of cloud amount and precipitation. On the whole, the surface energy fluxes exhibit a balance. During a phase of decreased precipitation, for example, day 340 – 360, T_g increase slightly. Both S_g and *SHF* are enhanced which almost offset each other. On the other hand, *LHF* decreases and $F_{IR}^{\uparrow}$ increases with increased T_g and reduced surface moisture. With $F_{IR}^{\downarrow}$ having a π/2 phase difference with precipitation, the surface energy fluxes almost offset to make surface energy budget balance.

From an energetics point of view, to make the surface energy budget balance, change in the surface energy flux due to enhanced or reduced precipitation must be compensated by changes in other surface energy fluxes. This energy balance is achieved, from a dynamical point of view, by adjusting the atmosphere to a new structure to be compatible with the new energetics constraints through the dynamics and thermodynamics operating within the atmosphere. From our analysis, it is the surface energetics constraint that operates to maintain the intraseasonal oscillation in the land-atmosphere system over Amazon.

5. Summary and discussion

The NCAR regional climate model version 2 (RegCM2) is used to investigate the observed characteristics of intraseasonal oscillations over South America. Our study is mainly concentrated on an intraseaonal mode, which is observed to account for a large portion of the intraseasonal variation, to have a standing feature and to be independent of

the MJO. The NCEP/DOE AMIP-II reanalysis is utilized to provide initial and lateral boundary conditions for the RegCM2 based upon the 00Z, 06Z, 12Z and 18Z data. The SST is taken from the extended reconstructed SST data of NOAA/NCDC.

The control experiment and a series of sensitivity experiments are designed and carried out. The sensitivity experiments are constructed in a way to gradually isolate the major factors responsible for the intraseasonal mode. They include the experiments of (1) the disturbances from outside of model domain being eliminated, (2) convective-radiative interaction in the atmosphere being excluded, (3) annual and daily cycles not operating in the model, (4) only one of annual and daily cycles being allowed, and (5) no interactions between atmosphere and surface forcing.

Our results indicate that the intraseasonal oscillation still exists with time-averaged lateral boundary condition, which prevents the MJO and other outside disturbances from entering the model's domain, suggesting a locally forced oscillation responsible for the intraseasonal mode independent of the MJO. Further experiments show that the annual and daily variabilities and radiative-convective interaction are not essential to the locally forced intraseasonal oscillation. The intraseasonal oscillations over Amazon in our model essentially result from interactions among atmospheric dynamical processes, surface radiation, the surface sensible and latent heat fluxes, and cumulus convection. The wavelet analyses of various surface energy fluxes and surface energy budget also verify that the primary cause of intraseasonal oscillation is the interaction of the land surface processes with the atmosphere.

In the present paper, we present evidence that an intraseasonal mode over Amazon, which has an observational counterpart, can result from land surface forcing and feedback from the atmosphere. We do not deny that the large-scale motion associated with the Madden-Julian oscillation can affect the intraseasonal oscillations over South America. At least to some extent, our modeling results can produce the observed oscillations and offer an essential direction to fully interpret them. The questions, such as, how the intraseasonal oscillation can arise in such a system, what determines the period of the oscillation and what condition favors them and so forth, still remain unanswered. Many more numerical experiments, and most essentially, theoretical analyses are needed in order to answer those questions.

Acknowledgments: This work was supported by NASA Earth Science Division.

References

Chao, W. C. and L. Deng, 1998: Tropical intraseasonal oscillation, super cloud clusters, and cumulus convection schemes. Part II: 3D aqua-planet simulations. *J. Atmos. Sci.,* **55**, 690 - 709.

Cleveland, R. B., W. S. Cleveland, J. E. McRae, and I. Terpenning, 1990: Stl: A seasonal-trend decomposition procedure based on LOESS (with discussion). *J. Official Statistics,* **6**, 3 – 73.

Dickinson, R. E., A. Henderson-Sellers, and P. J. Kennedy, 1992: Biosphere-Atmosphere Transfer Scheme (BATS) version 1E as coupled to the NCAR Community Climate Model. NCAR Tech. Note NCAR/TN-387+STR, 72 pp.

Eltahir, E. A. B., and J. S. Pal, 1996: Relationship between surface conditions and subsequent rainfall in convective storms. *J. Geophys. Res.,* **101**, 26,237 – 26,245.

Fu, R., R. E. Dickinson, M. Chen, and H. Wang, 2001: How do tropical sea surface temperatures influence the seasonal distribution of precipitation in the equatorial Amazon? *J. Climate,* **14**, 4003 – 4026.

Giorgi, F., M. R. Marinucci and G. T. Bates, 1993a: Development of a second generation regional climate (RegCM2): Boundary layer and radiative transfer processes. *Mon. Wea. Rew.* **121**, 2794 – 2813.

Giorgi, F., M. R. Marinucci and G. T. Bates, 1993b: Development of a second generation regional climate (RegCM2): Convective processes and assimilation of lateral boundary conditions. *Mon. Wea. Rew.* **121,** 2814-2832.

Giorgi, F. and L. O. Mearns, 1999: Introduction to special section: Regional climate modeling revisited, *J. Geophys. Res.,* **104**, 6335 – 6352.

Ghil M. et al., 2001: Advanced spectral methods for climatic time series, *Reviews of Geophysics*, **40**, **1**-1 – **1**-41.

Grell G. A., J. Dudhia, and D. R. Stauffer 1994: A description of the fifth generation Penn State/NCAR Mesoscale Model (MM5). NCAR Tech. Note NCAR/TN-398+STR, 121pp.

Hayashi, Y., and D. G. Golder, 1993: Tropical 40-50- and 25-30-day oscillations appearing in realistic and idealized GFDL climate models and the ECMWF dataset. *J. Atmos. Sci.,* **50**, 464-494.

Holtslag A. A. M., E. I. E. de Bruijn, and H. L. Pan 1990: A high resolution air mass transformation model for short-range weather forecasting. *Mon. Wea. Rev.* **118**: 1561-1575.

Hu, Q. and D. A. Randall, 1994: Low-frequency oscillations in radiative-convective systems. *J. Atmos. Sci.*, **51**, 1089 – 1099.

Hu, Q. and D. A. Randall, 1995: Low-frequency oscillations in radiative-convective systems. Part II: An idealized model. *J. Atmos. Sci.*, **52**, 478 – 490.

Kanamitsu, M. and Coauthors, 2002: NCEP-DOE AMIP-II Reanalysis. *Bull. Amer. Meteor. Soc.,* **83**, 1631 – 1643.

Kalnay, E., and Coauthors, 1996: The NCEP/NCAR 40-Year Reanalysis Project. *Bull. Amer. Meteor. Soc.,***77**, 437 – 471.

Liebmann, B., G. N. Kiladis, J. A. Marengo, T. Ambrizzi, and J. D. Glick, 1999: Submonthly convective variability over South America and South Atlantic convergence zone. *J. Climate,* **12**, 1877 – 1891.

Madden, R. A., and P. R. Julian, 1994: Observations of the 40-50-day tropical oscillation-A review, *Mon. Wea. Rev.,* **122**, 814 – 837.

Nicolini, M., P. Salio, J. J. Katzfey, J. L. McGregor, and A. C. Saulo, 2002: January and July regional climate simulation over South America, *J. Geophys. Res.,* **107**, 4637 – 4649.

Paegle, J. N., L. A. Byerle, and K. C. Mo, 2000: Intraseasonal modulation of South American summer precipitation. *Mon. Wea. Rev.,* **128**, 837 – 850.

Pal, J. S., E. E. Small, and E. A. B. Eltahir, 2000: Simulation of regional-scale water and energy budgets: Representation of subgrid cloud and precipitation processes with RegCM, *J. Geophys. Res.,* **105**, 29,579 – 29,594.

Smith, T. M., and R. W. Reynolds, 2003: Extended reconstruction of global sea surface temperatures based on COADS data (1854-1997). *J. Climate,* **16**, 1495-1510.

Seth, A., and M. Rojas, 2003: Simulation and sensitivity in a nest modeling system for South America. Part I: reanalyses boundary forcing. *J. Climate,* **16**, 2437-2452.

Torrence, C., and G. P. Compo, 1998: A Practical Guide to Wavelet Analysis. *Bull. Amer. Meteor. Soc.*, **9**, 61-78.

Xie, P., and P. A. Arkin, 1996: Analyses of global monthly precipitation using gauge observations, satellite estimates, and numerical model predictions. *J. Climate,* **9**, 840-858.

Zhou, J. and K. M. Lau, 1998: Does a monsoon climate exist over South America? *J. Climate,* **11**, 1020-1040.

Zhou, J. and K. M. Lau, 2002: Summertime intraseasonal variability over South America, Reprint, *24th Annual Climate Diagnostics and Prediction Workshop,* Tucson, AZ.

Captions

Table 1. Summary of the experiments performed.

Fig. 1. Model domain and topography (units are 100m). Also shown is the area selected for analysis.

Fig. 2. December – March mean precipitation for (a) the control run and (b) the CMAP data.

Fig. 3a. Time series of the mean precipitation in the Amazon region for the control experiment (thin line) and seasonal trend (thick line).

Fig. 3b. Time series of precipitation with the trend removed (thin line) and reconstructed time series of precipitation anomaly based on the SSA (thick line) for the control experiment.

Fig. 3c. Singular spectrum of the precipitation for the control experiment.

Fig. 3d. MEM spectrum of reconstructed time series of precipitation for the control experiment.

Fig. 4a. The same as Fig. 3a but for CBC experiment.

Fig. 4b. The same as Fig. 3d but for CBC experiment.

Fig. 5a. The same as Fig. 3a but for CRD experiment.

Fig. 5b. The same as Fig. 3d but for CRD experiment.

Fig. 6a. The same as Fig. 3d but for NZEN experiment.

Fig. 6b. The same as Fig. 3d but for NDIA experiment.

Fig. 6c. The same as Fig. 3d but for NANU experiment.

Fig. 7. The same as Fig. 3a but for WSUF experiment.

Fig.8. Normalized local wavelet power spectrum of the precipitation for CRD experiment.

Fig. 9a. Wavelet power spectrum of T_g and its time series for CRD experiment.

Fig. 9b. The same as Fig. 9a but for S_g.

Fig. 9c. The same as Fig. 9a but for $F_{IR}^{\downarrow}$.

Fig. 9d. The same as Fig. 9a but for $F_{IR}^{\uparrow}$.

Fig. 9e. The same as Fig. 9a but for *SHF*.

Fig. 9f. The same as Fig. 9b but for *LHF*.

Fig. 10. Time series of filtered precipitation, T_g, S_g, $F_{IR}^{\downarrow}$, $F_{IR}^{\uparrow}$, *SHF* and *LHF* between day 320 and day 380 for CRD experiment.

	Lateral boundary conditions	Long- and short-wave radiative heating rate in the atmosphere	Daily variation in the surface radiation	Annual variation in the surface radiation	Land surface energy exchange
CNTRL	Varying	Varying	Yes	Yes	Yes
CBC	Fixed	Varying	Yes	Yes	Yes
CRD	Fixed	Fixed	Yes	Yes	Yes
NZEN	Fixed	Fixed	No	No	Yes
NDIA	Fixed	Fixed	No	Yes	Yes
NANU	Fixed	Fixed	Yes	No	Yes
WSFC	Fixed	Fixed	No	No	No

Table 1

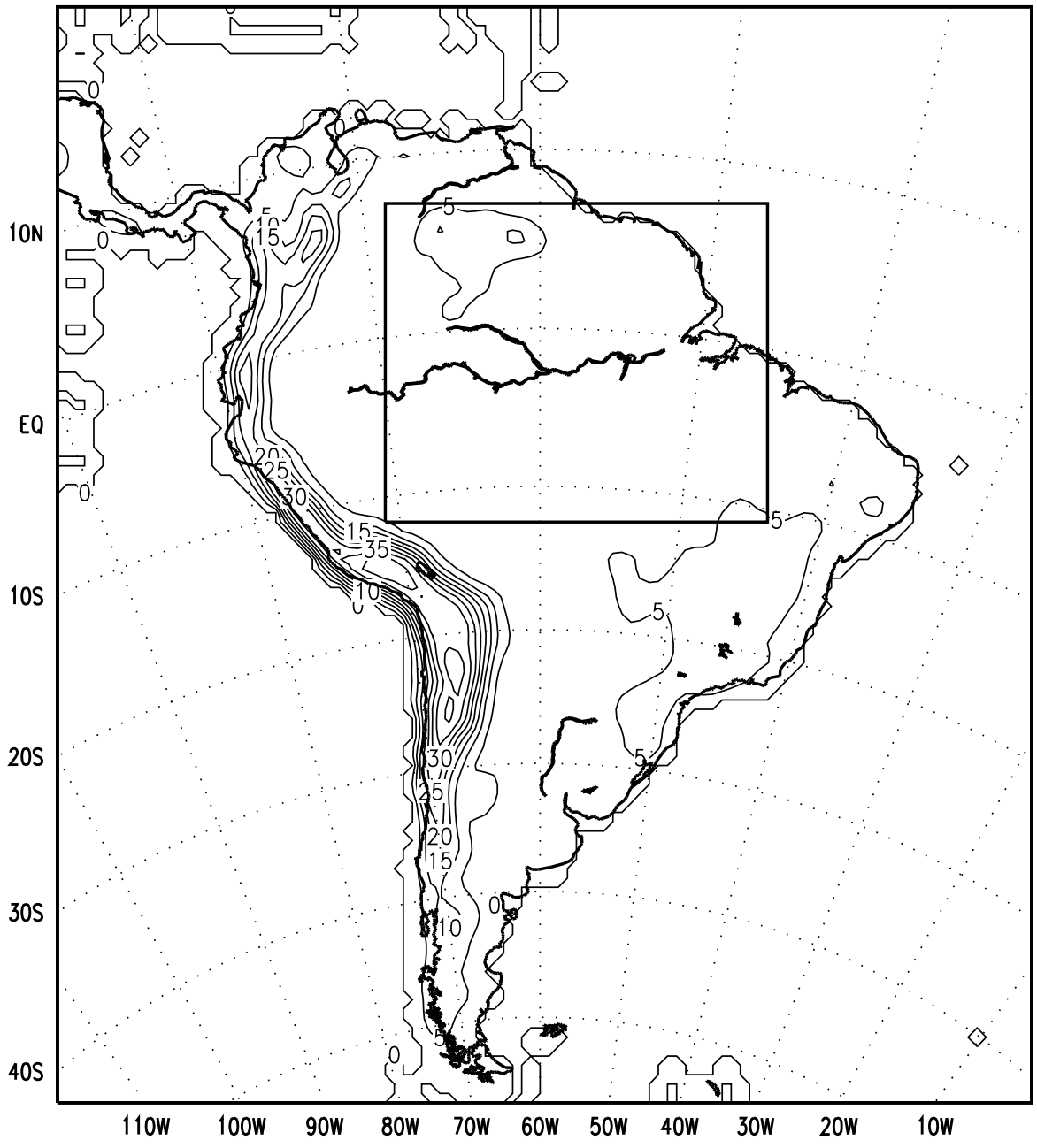
10N
EQ
10S
20S
30S
40S
110W
100W
90W
80W
70W
60W
50W
40W
30W
20W
10W

Fig. 1

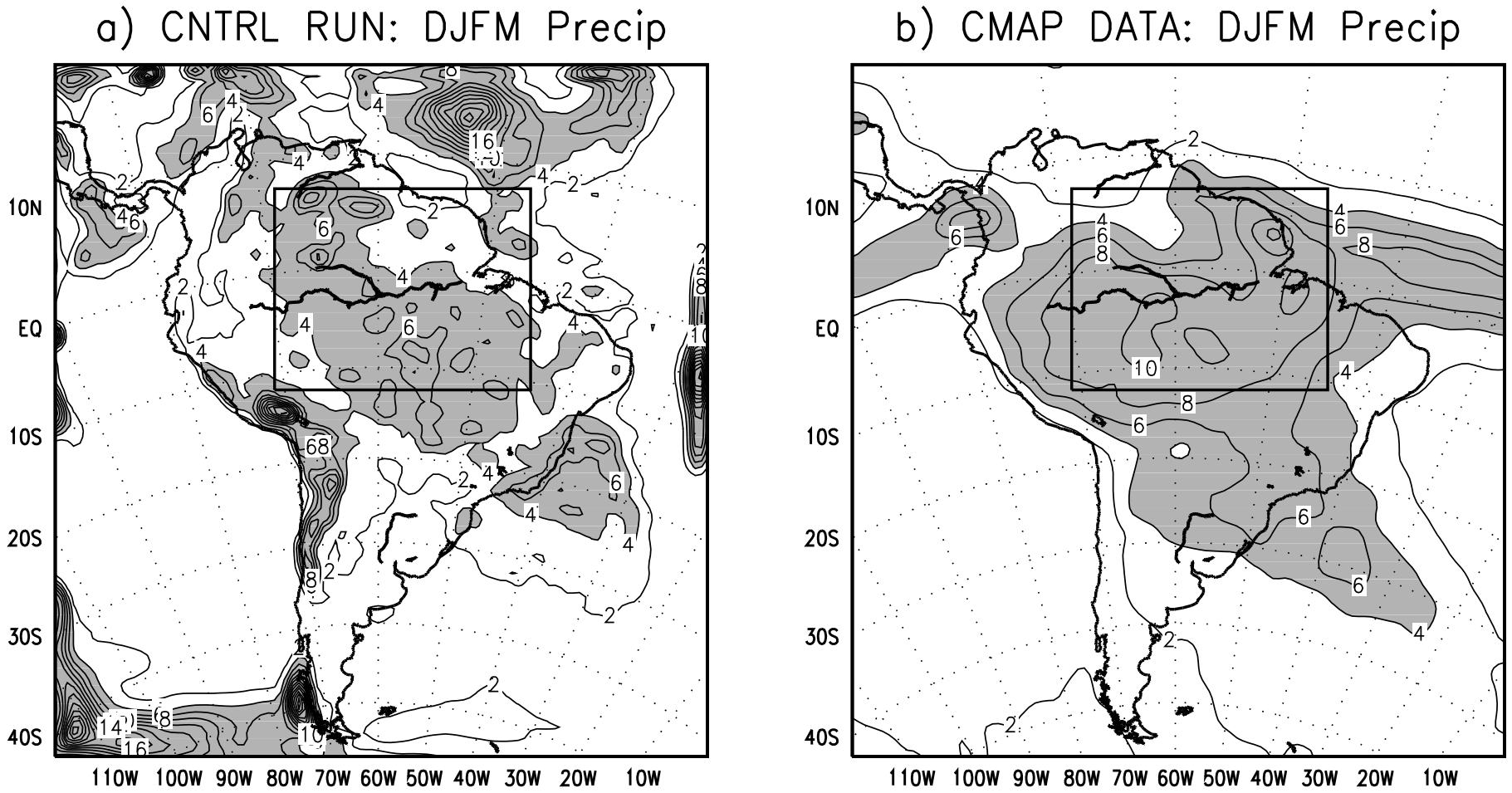
a) CNTRL RUN: DJFM Precip
b) CMAP DATA: DJFM Precip
10N
EQ
10S
20S
30S
40S
110W 100W 90W 80W 70W 60W 50W 40W 30W 20W 10W

Fig. 2

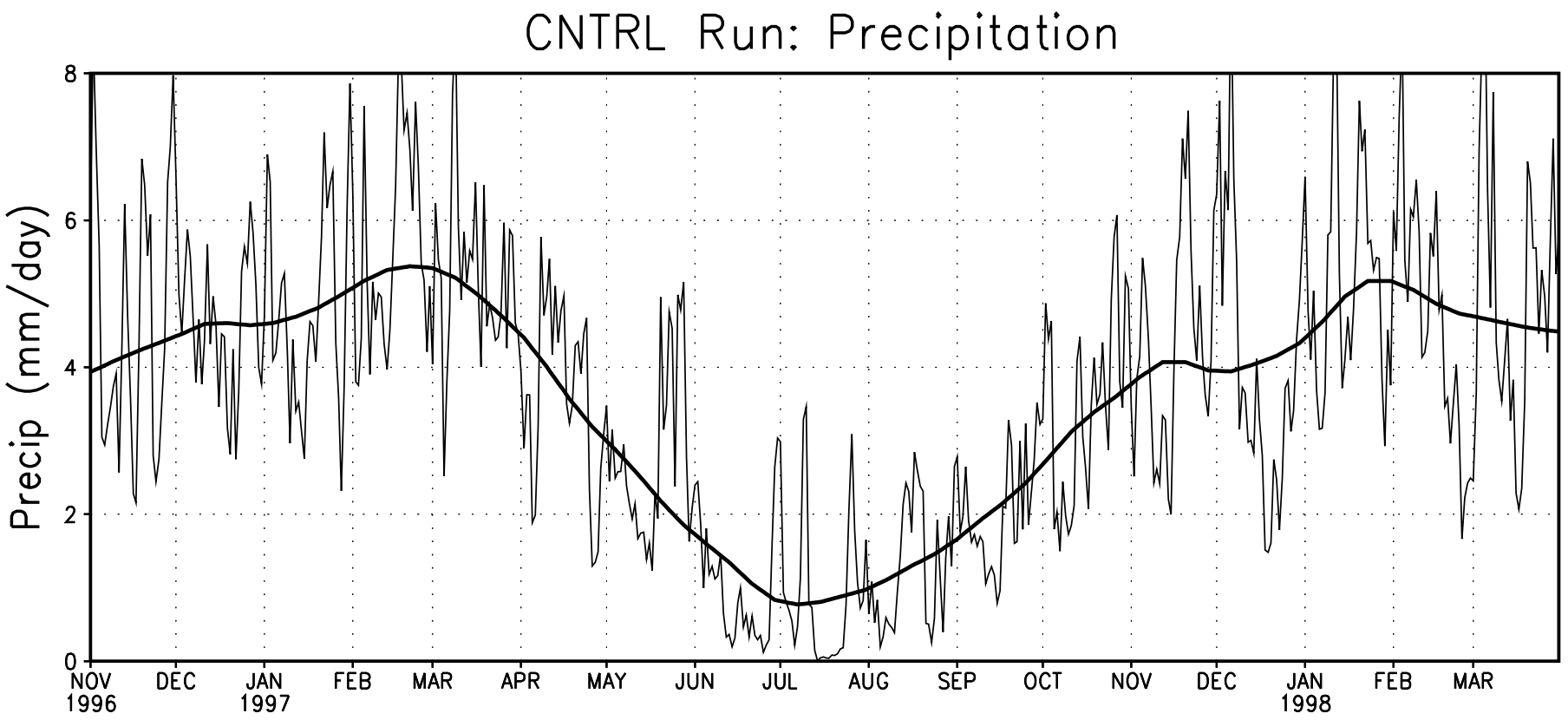
CNTRL Run: Precipitation
Precip (mm/day)
0
2
4
6
8
NOV
1996
DEC
JAN
1997
FEB
MAR
APR
MAY
JUN
JUL
AUG
SEP
OCT
NOV
DEC
JAN
1998
FEB
MAR

Fig. 3a

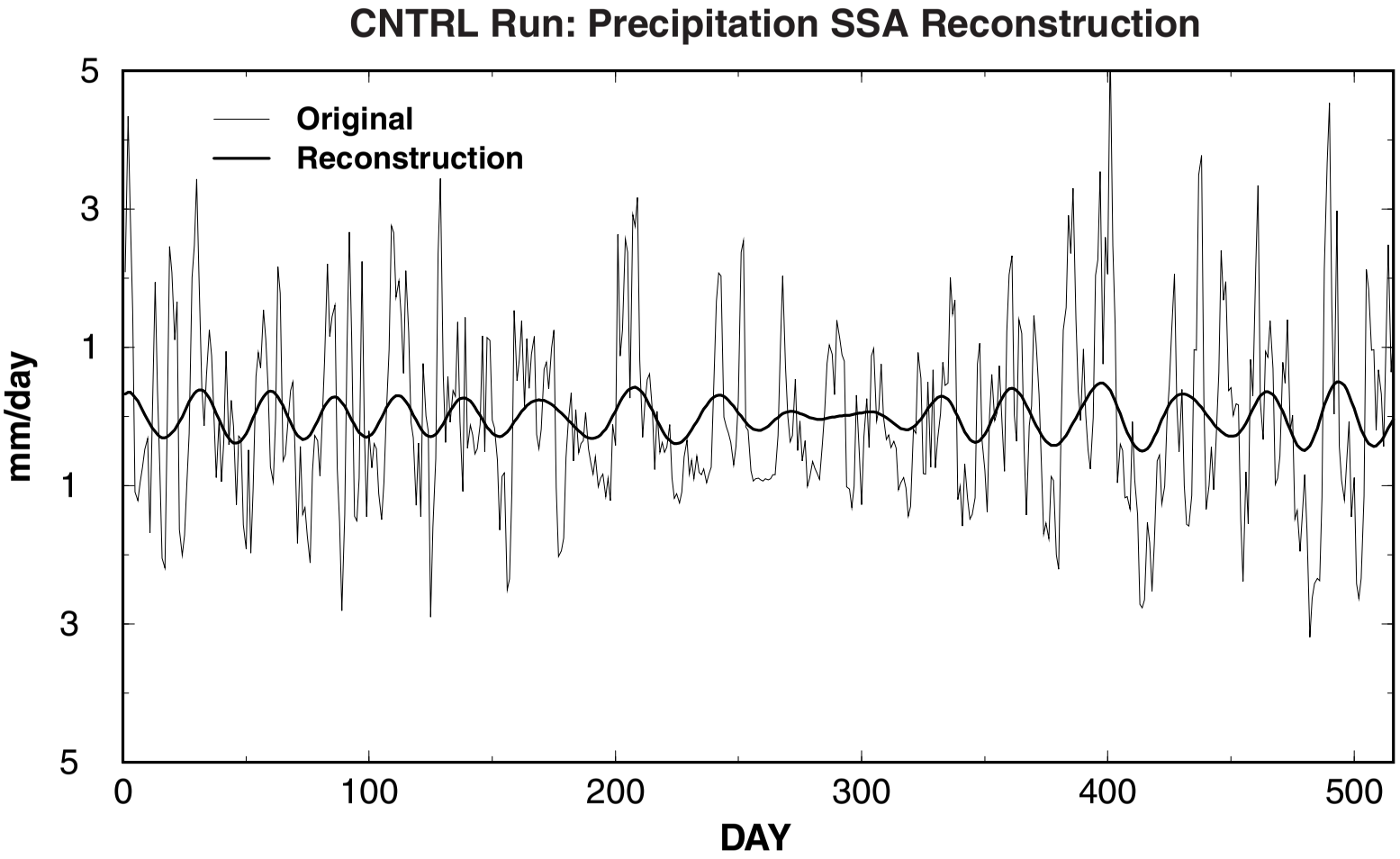
CNTRL Run: Precipitation SSA Reconstruction
Original
Reconstruction
mm/day
5
3
1
1
3
5
0
100
200
300
400
500
DAY

Fig. 3b

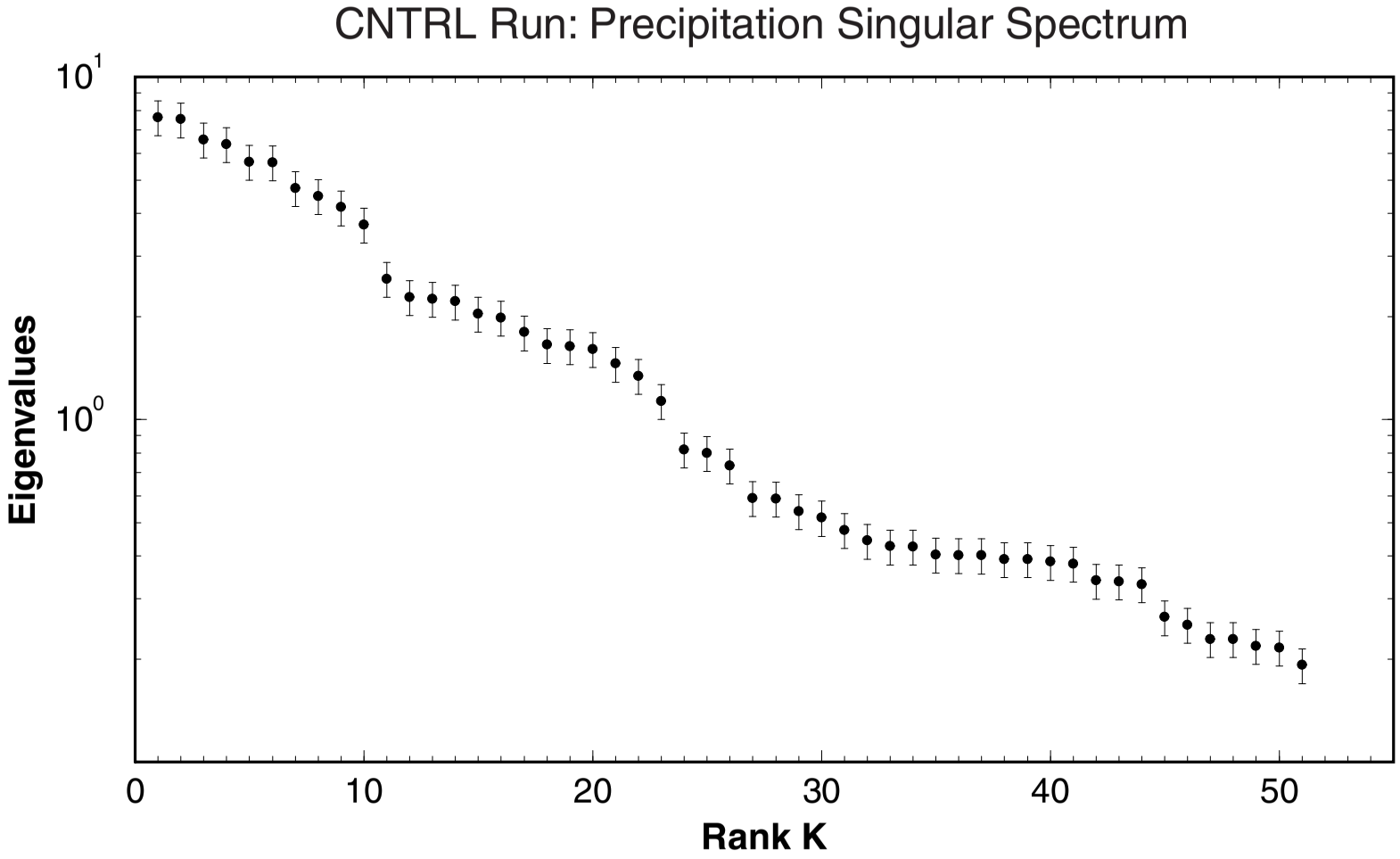
CNTRL Run: Precipitation Singular Spectrum
Eigenvalues
10^1
10^0
0
10
20
30
40
50
Rank K

Fig. 3c

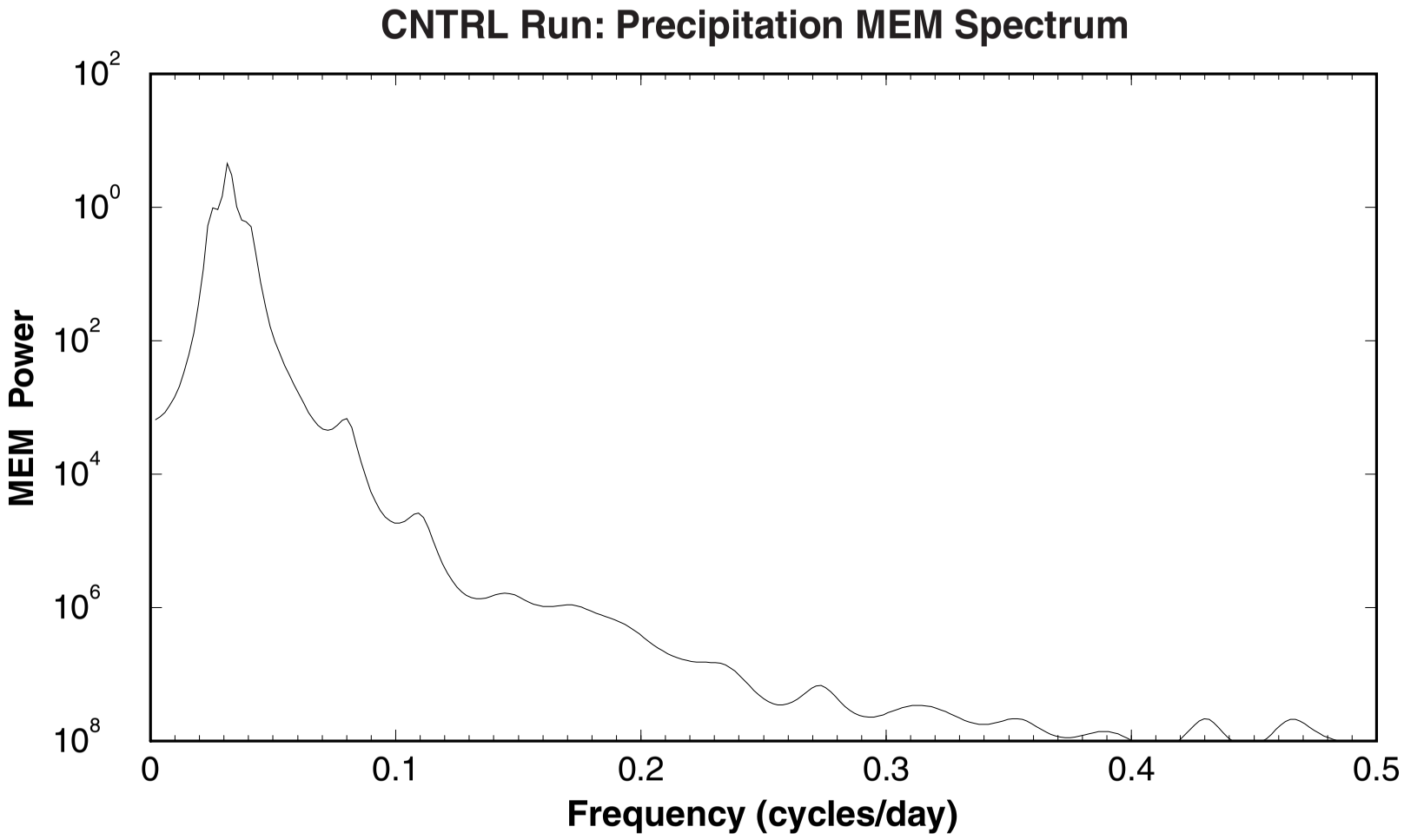
CNTRL Run: Precipitation MEM Spectrum
MEM Power
10^2
10^0
10^2
10^4
10^6
10^8
0
0.1
0.2
0.3
0.4
0.5
Frequency (cycles/day)

Fig. 3d

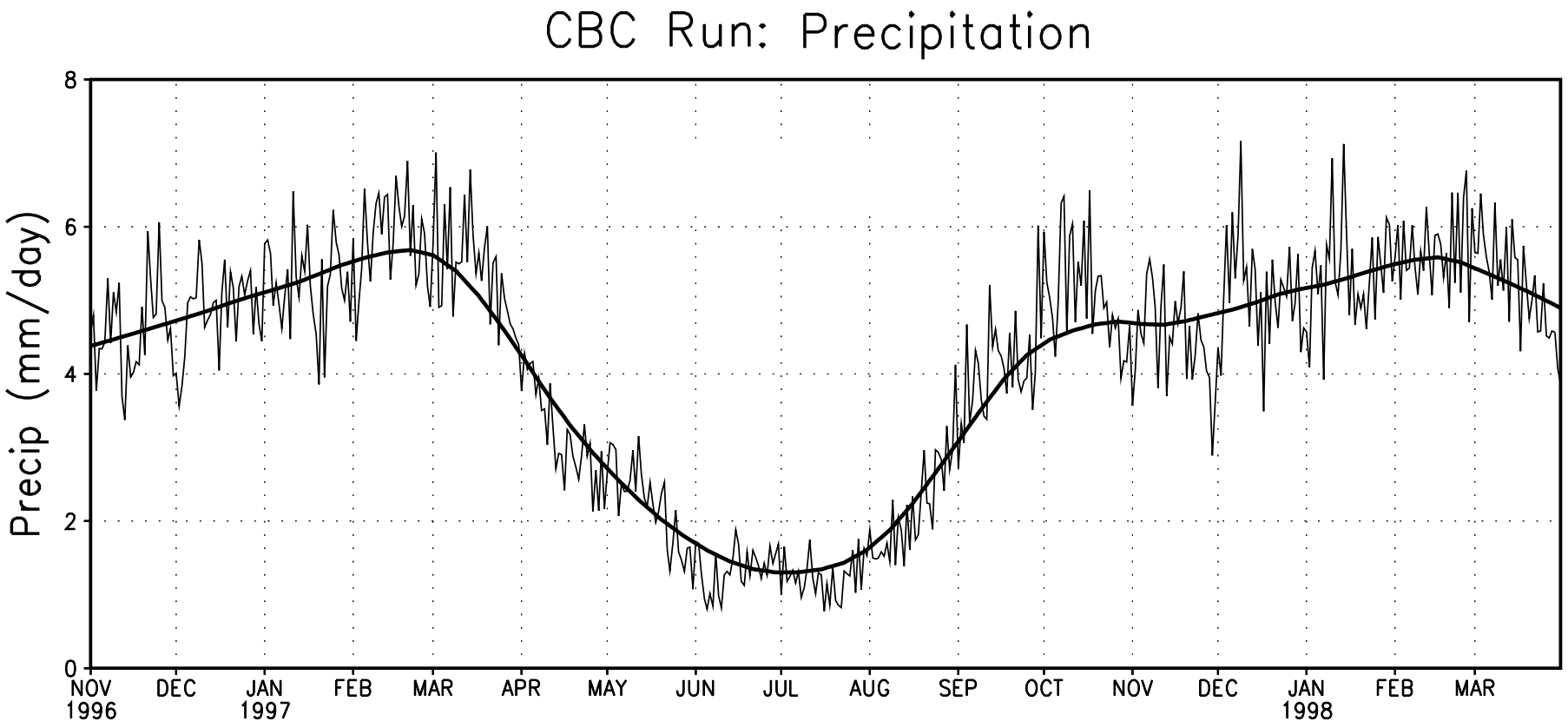
CBC Run: Precipitation
Precip (mm/day)
0
2
4
6
8
NOV
1996
DEC
JAN
1997
FEB
MAR
APR
MAY
JUN
JUL
AUG
SEP
OCT
NOV
DEC
JAN
1998
FEB
MAR

Fig. 4a

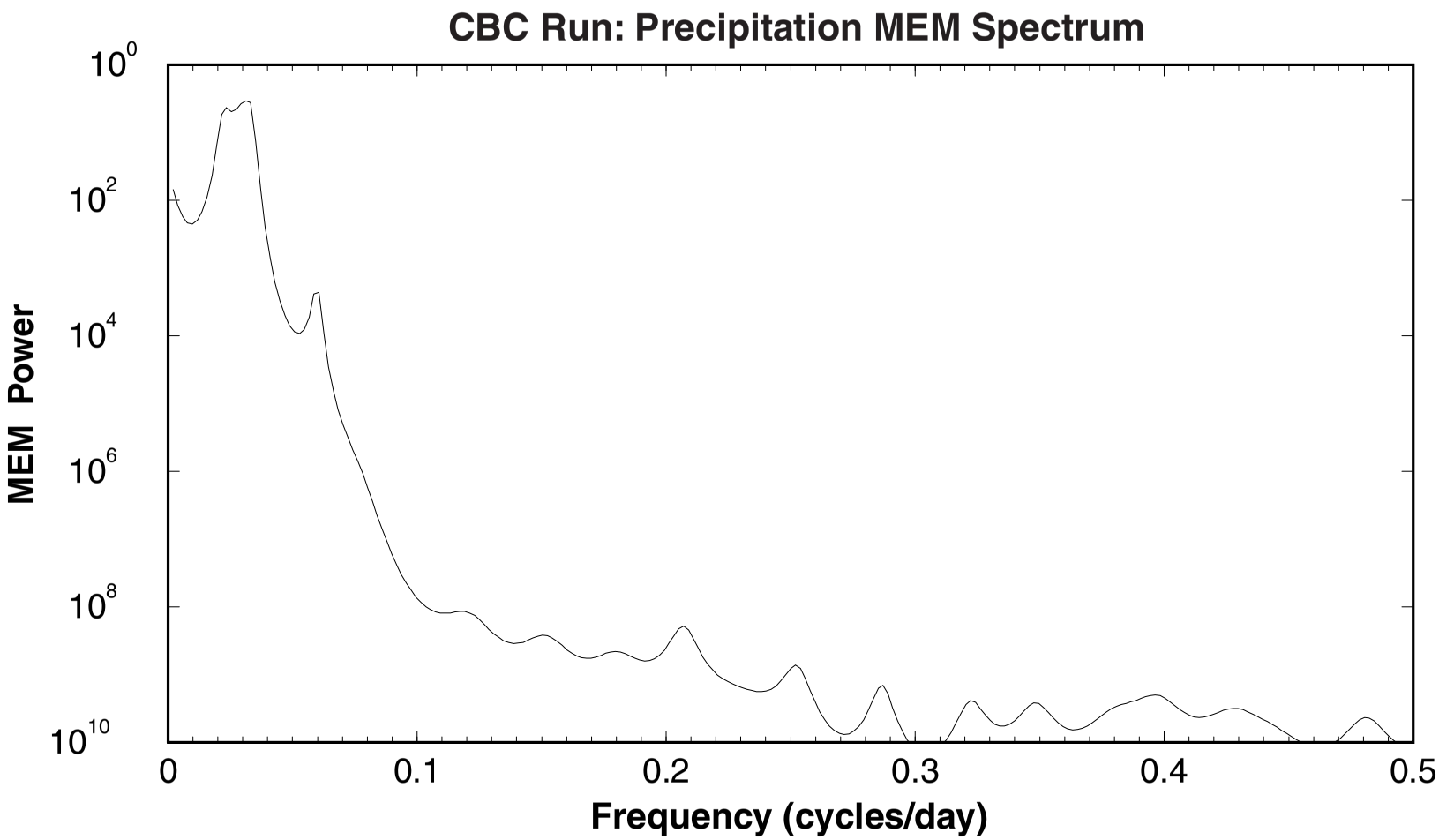
CBC Run: Precipitation MEM Spectrum
MEM Power
10^0
10^2
10^4
10^6
10^8
10^{10}
0
0.1
0.2
0.3
0.4
0.5
Frequency (cycles/day)

Fig. 4b

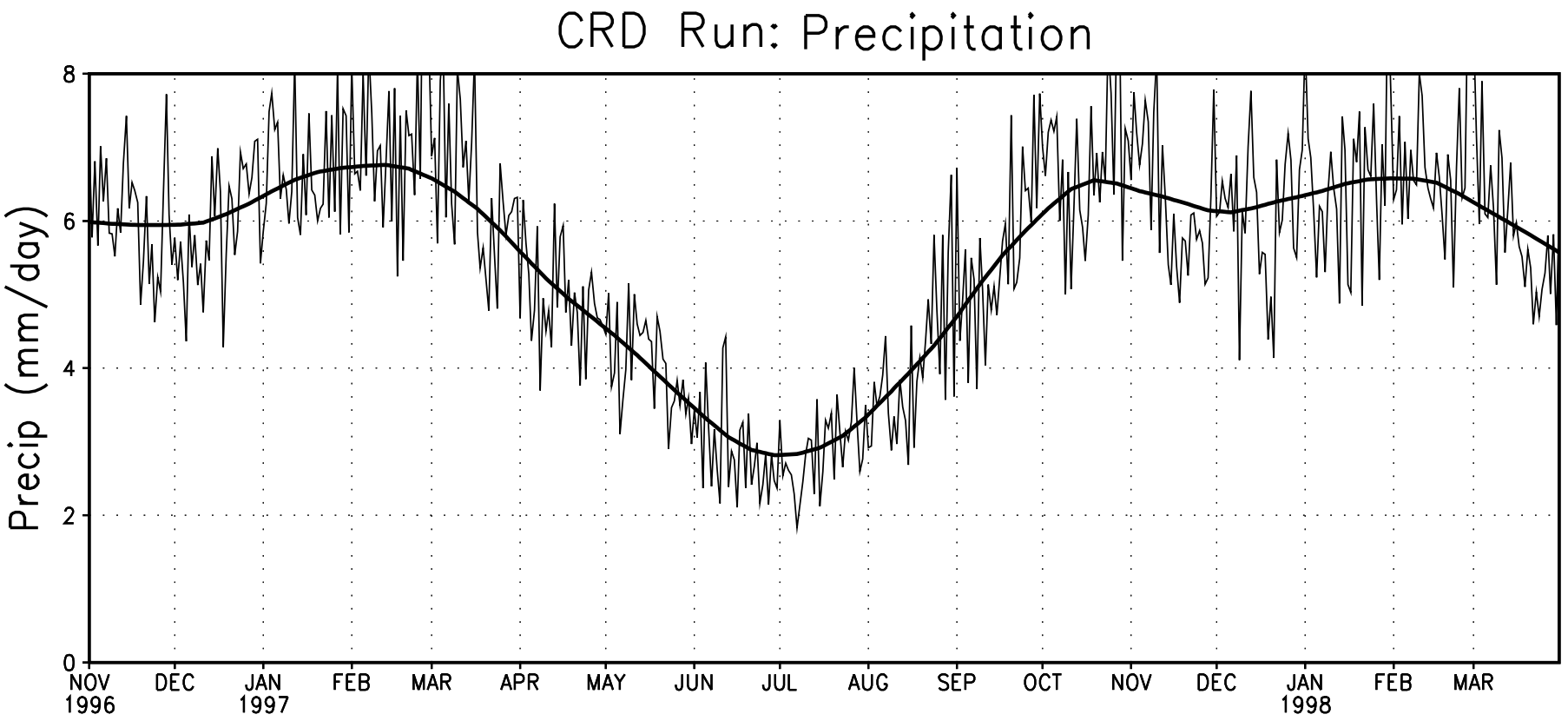
CRD Run: Precipitation
Precip (mm/day)
0
2
4
6
8
NOV
1996
DEC
JAN
1997
FEB
MAR
APR
MAY
JUN
JUL
AUG
SEP
OCT
NOV
DEC
JAN
1998
FEB
MAR

Fig. 5a

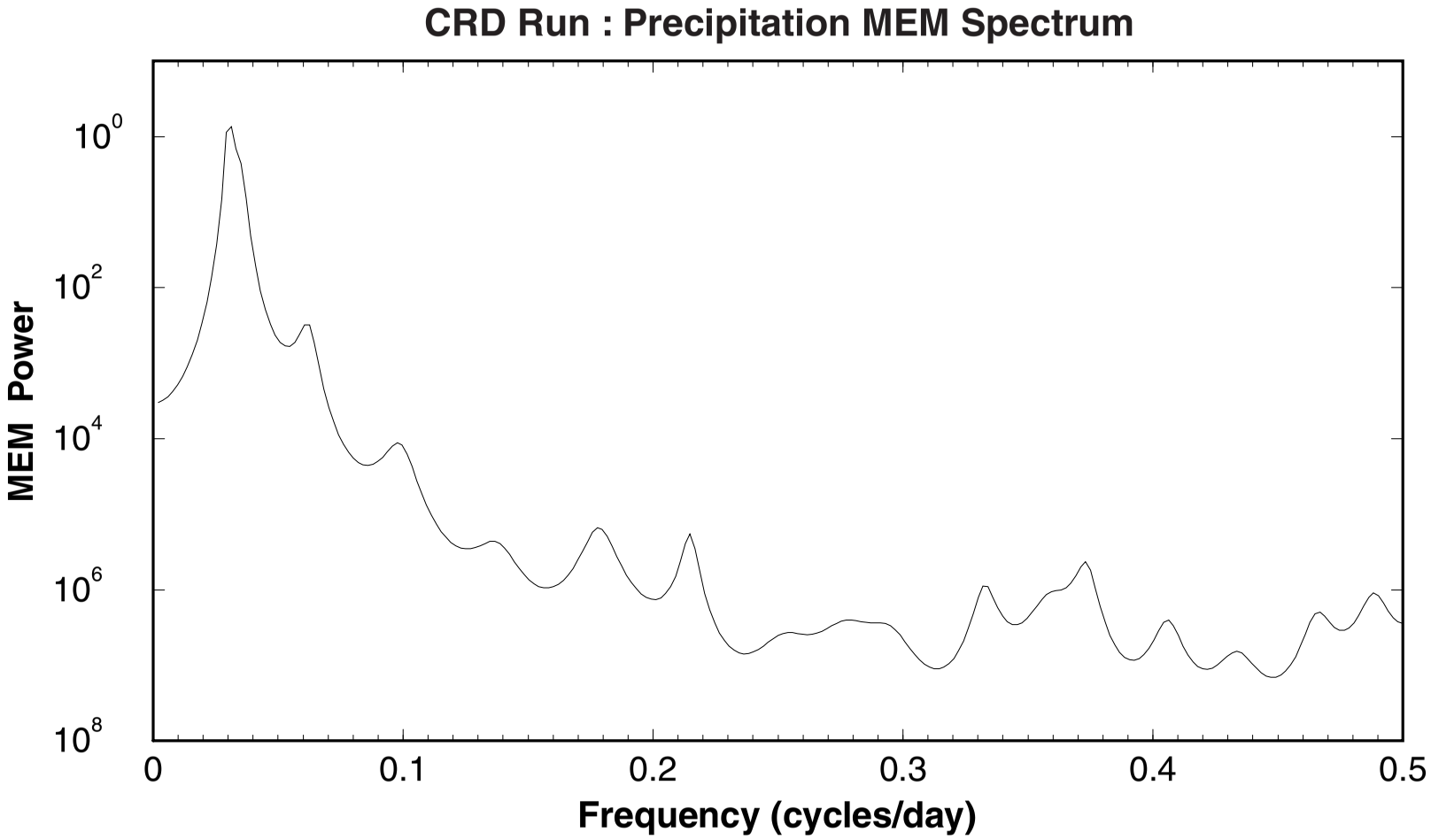
CRD Run : Precipitation MEM Spectrum
MEM Power
10^0
10^2
10^4
10^6
10^8
0
0.1
0.2
0.3
0.4
0.5
Frequency (cycles/day)

Fig. 5b

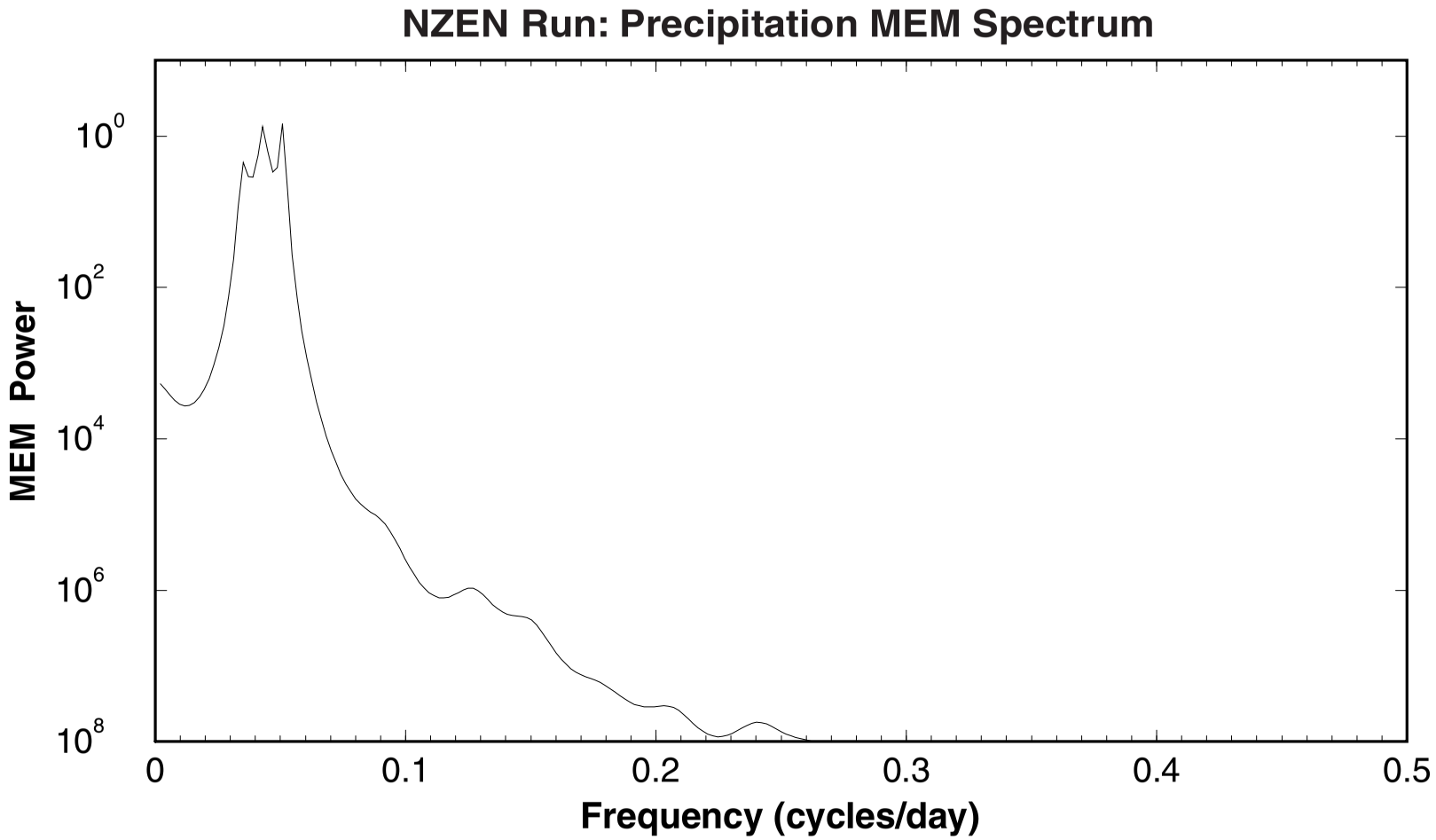
NZEN Run: Precipitation MEM Spectrum
MEM Power
10^0
10^2
10^4
10^6
10^8
0
0.1
0.2
0.3
0.4
0.5
Frequency (cycles/day)

Fig. 6a

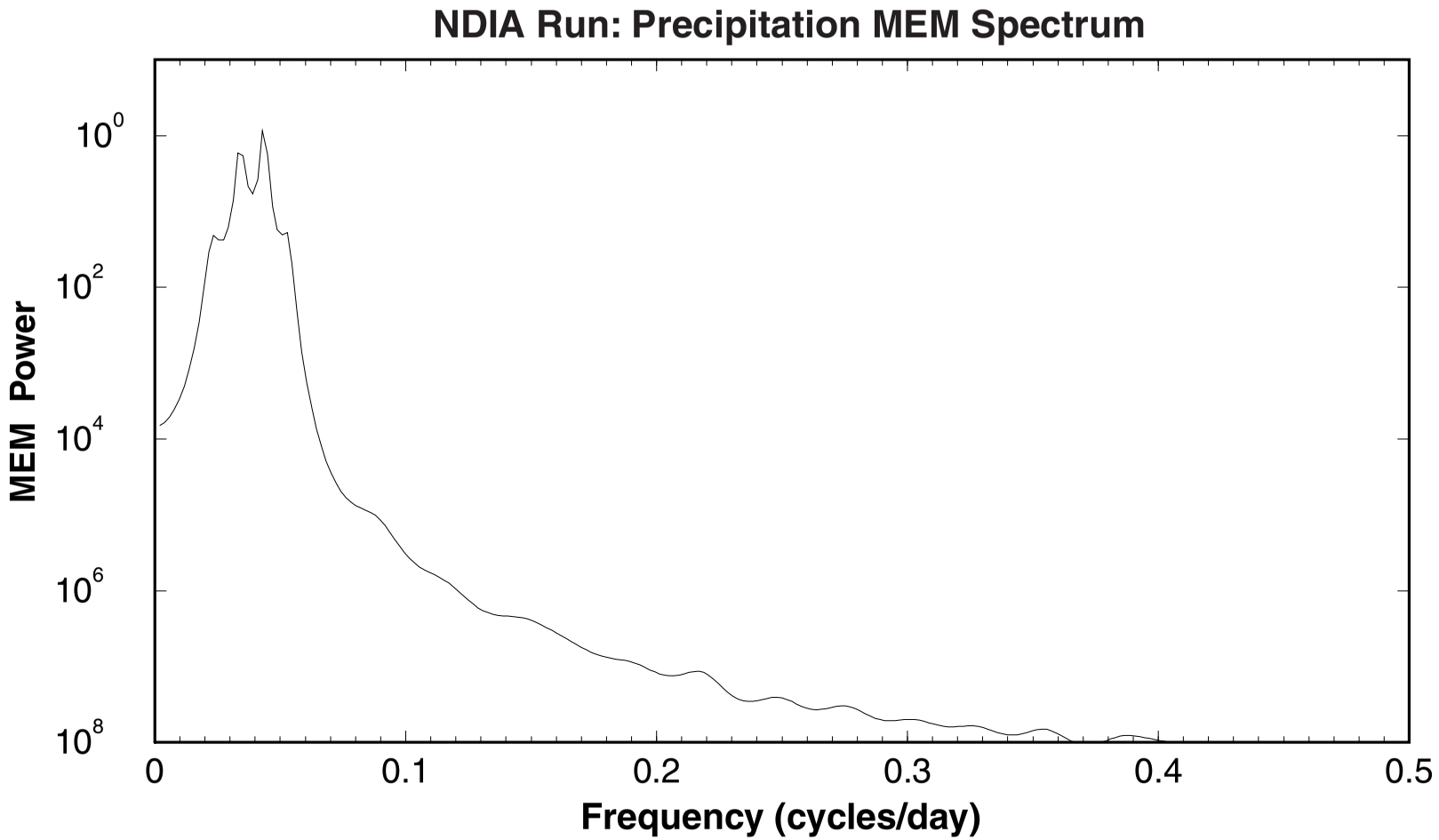
NDIA Run: Precipitation MEM Spectrum
MEM Power
10^0
10^2
10^4
10^6
10^8
0
0.1
0.2
0.3
0.4
0.5
Frequency (cycles/day)

Fig. 6b

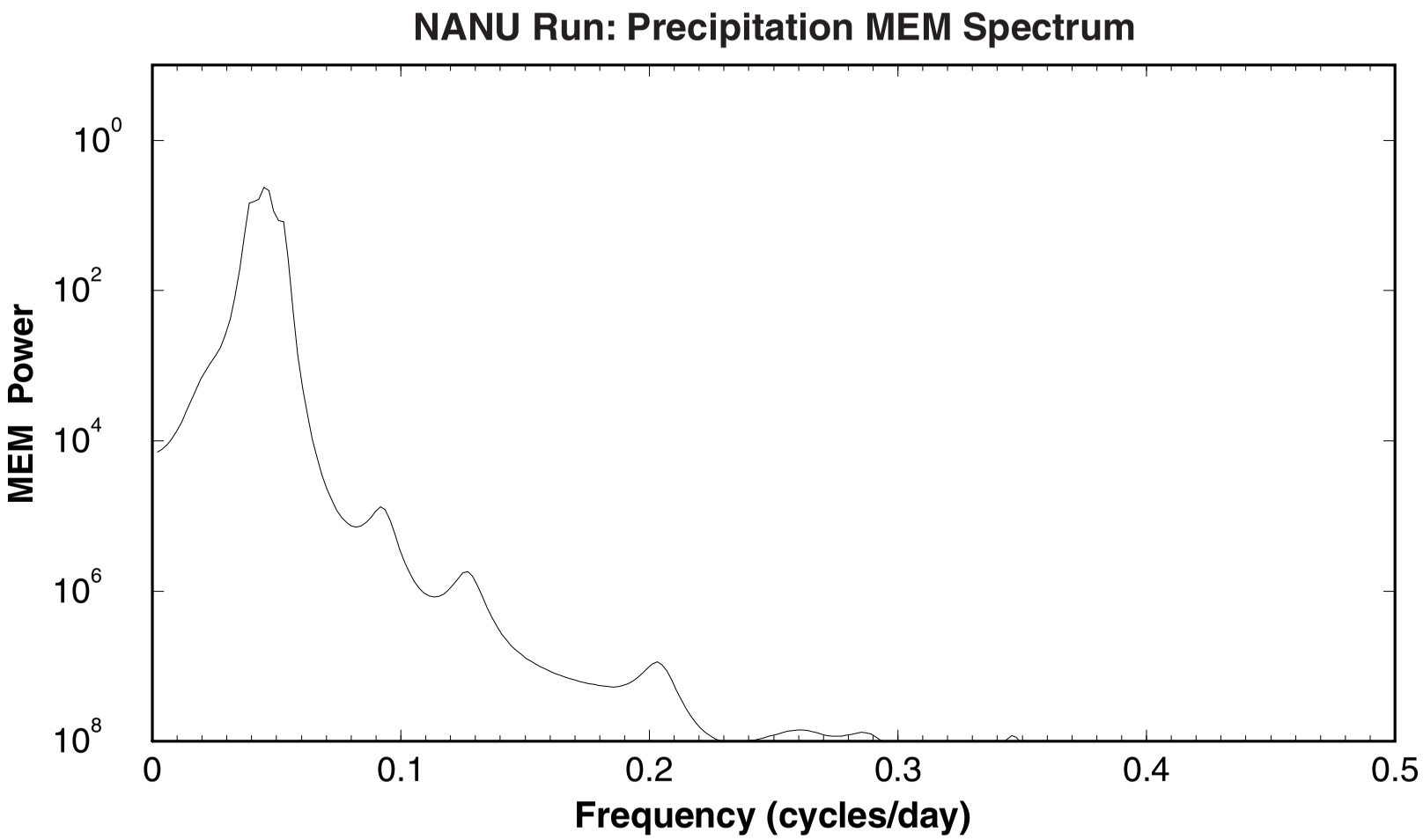
NANU Run: Precipitation MEM Spectrum
MEM Power
10^0
10^2
10^4
10^6
10^8
0
0.1
0.2
0.3
0.4
0.5
Frequency (cycles/day)

Fig. 6c

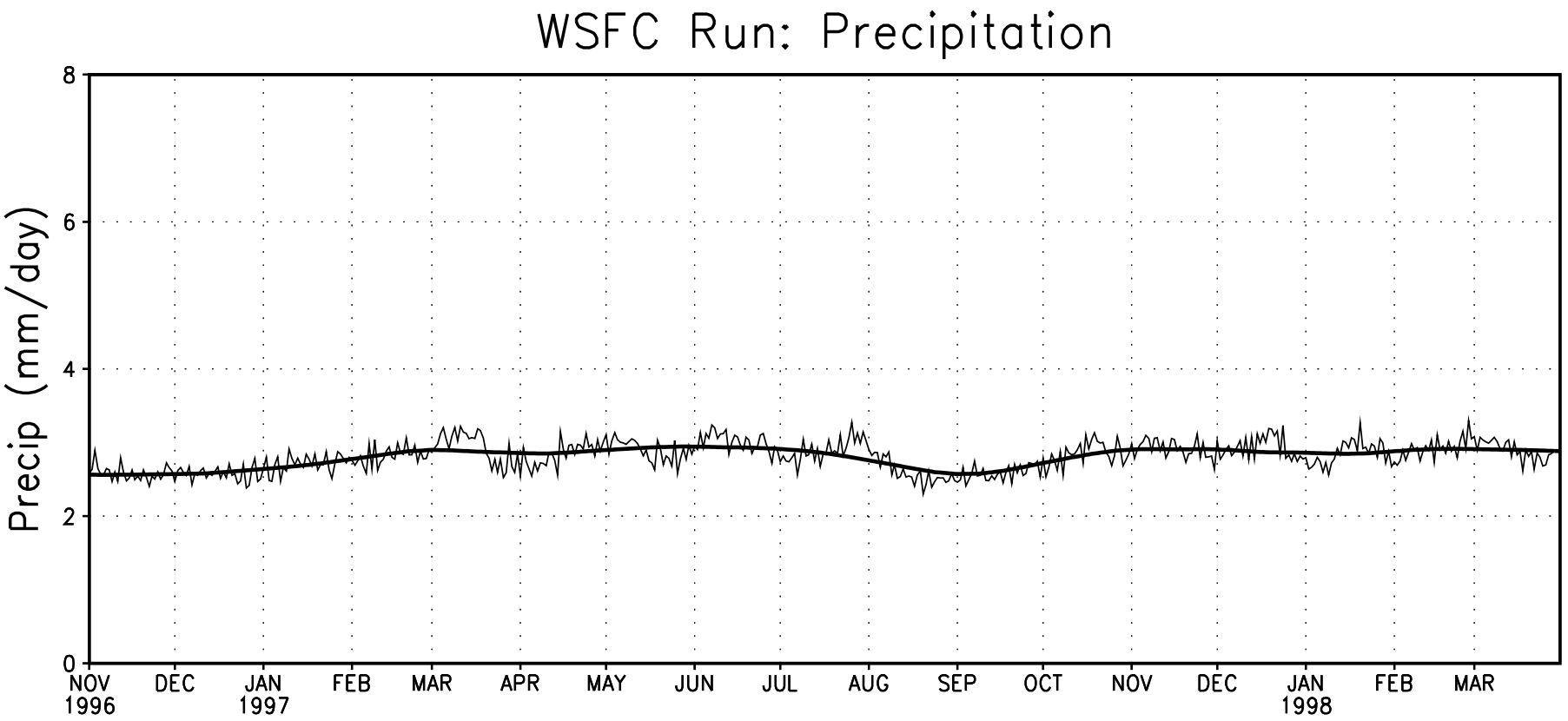
WSFC Run: Precipitation
Precip (mm/day)
8
6
4
2
0
NOV
1996
DEC
JAN
1997
FEB
MAR
APR
MAY
JUN
JUL
AUG
SEP
OCT
NOV
DEC
JAN
1998
FEB
MAR

Fig. 7

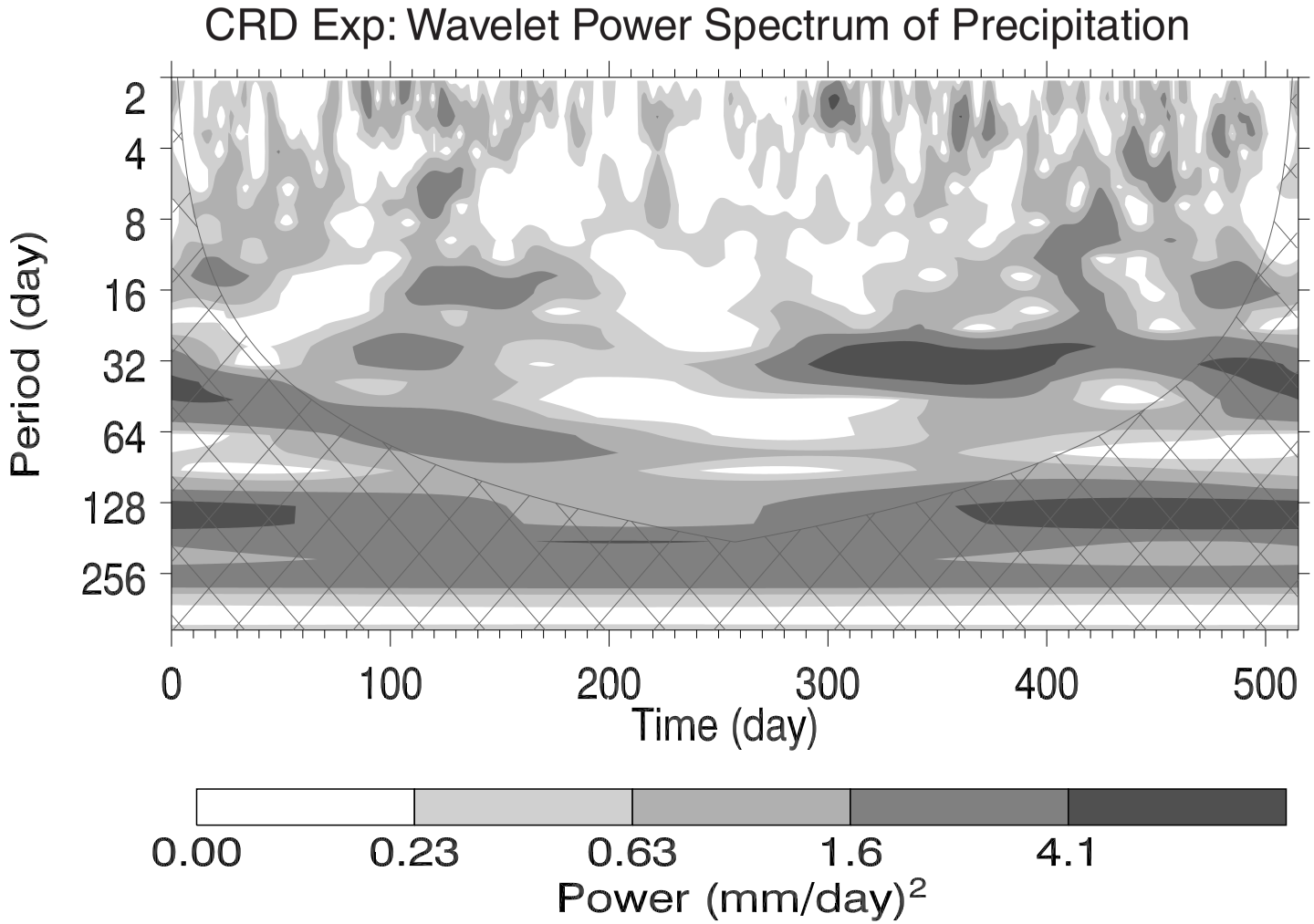
CRD Exp: Wavelet Power Spectrum of Precipitation
Period (day)
2
4
8
16
32
64
128
256
0
100
200
300
400
500
Time (day)
0.00
0.23
0.63
1.6
4.1
Power (mm/day)2

Fig. 8

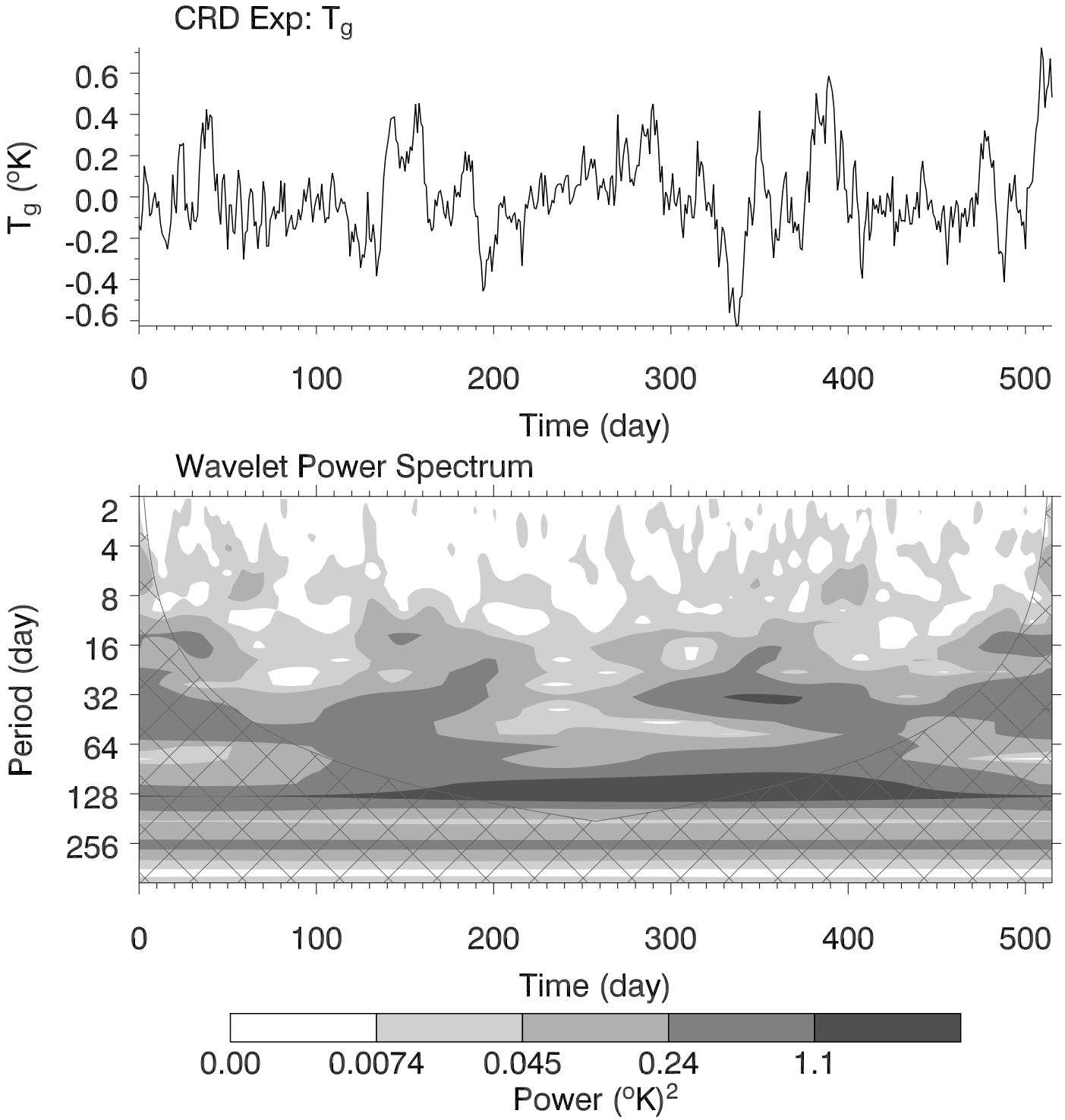
CRD Exp: T_g
T_g (°K)
0.6
0.4
0.2
0.0
-0.2
-0.4
-0.6
0
100
200
300
400
500
Time (day)
Wavelet Power Spectrum
Period (day)
2
4
8
16
32
64
128
256
0
100
200
300
400
500
Time (day)
0.00
0.0074
0.045
0.24
1.1
Power (°K)^2

Fig. 9a

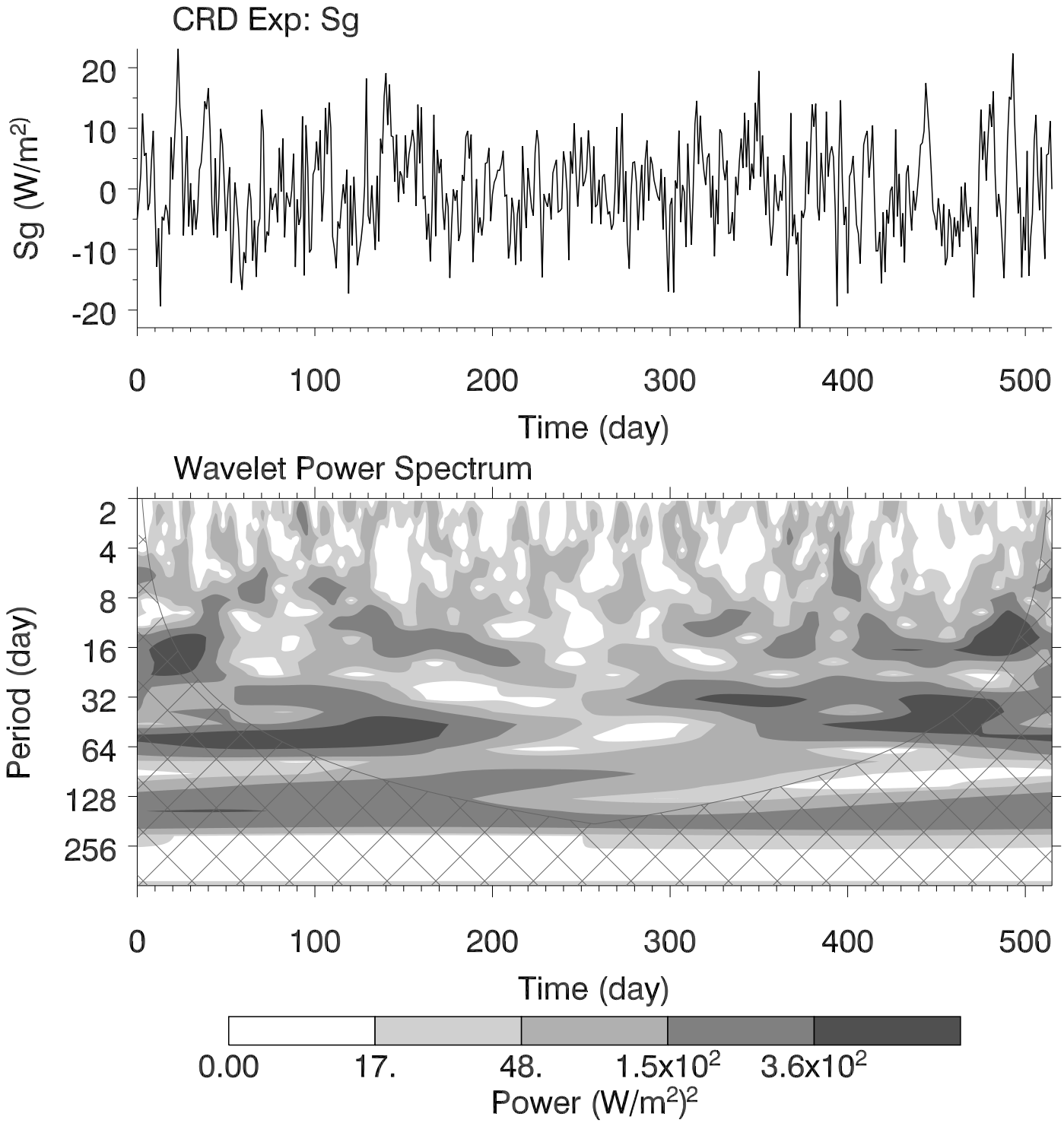
CRD Exp: Sg
Sg (W/m2)
20
10
0
-10
-20
0
100
200
300
400
500
Time (day)
Wavelet Power Spectrum
Period (day)
2
4
8
16
32
64
128
256
0
100
200
300
400
500
Time (day)
0.00
17.
48.
1.5x10^2
3.6x10^2
Power (W/m2)2

Fig. 9b

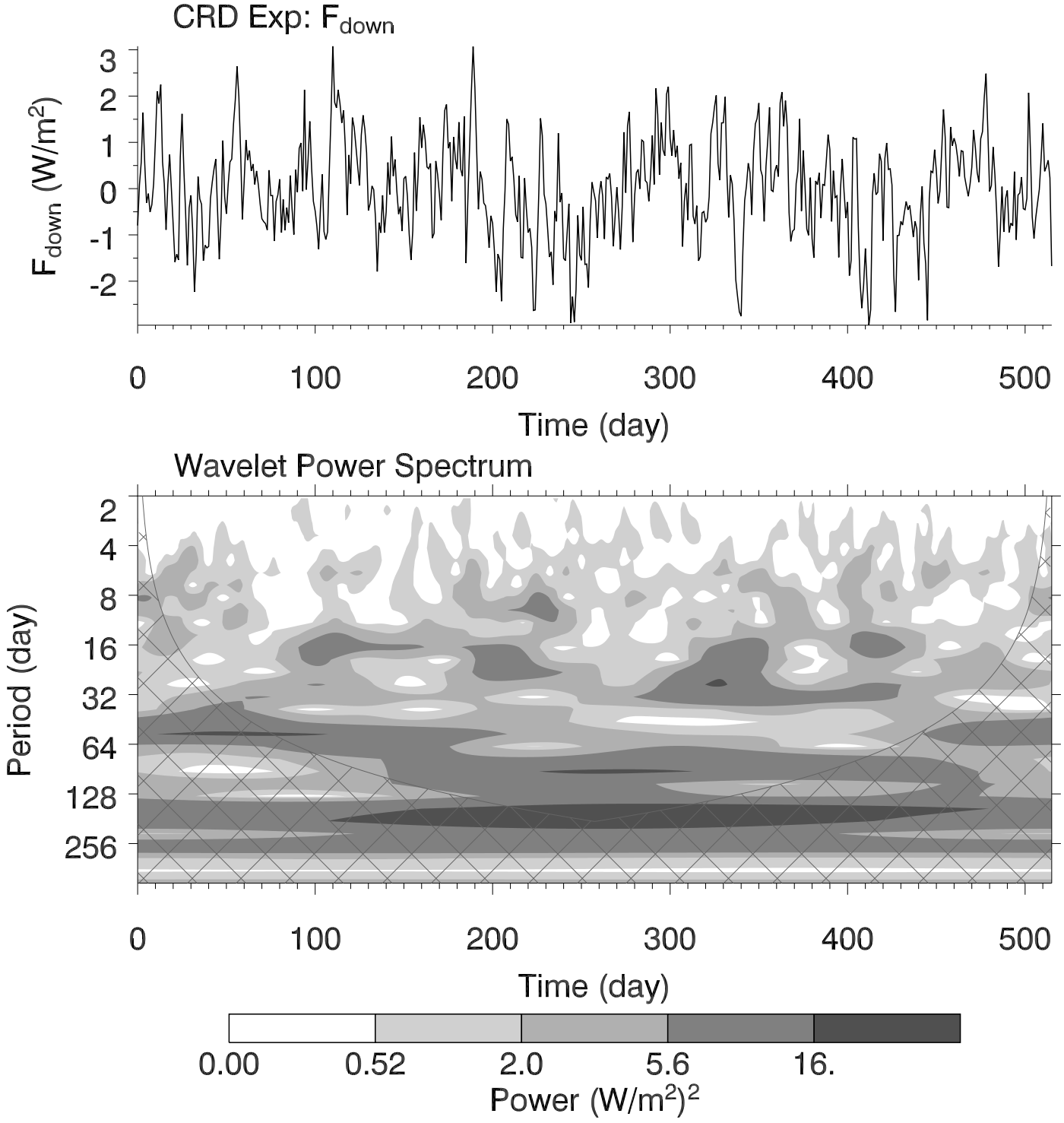
CRD Exp: F_{down}
F_{down} (W/m^2)
3
2
1
0
-1
-2
0
100
200
300
400
500
Time (day)
Wavelet Power Spectrum
Period (day)
2
4
8
16
32
64
128
256
0
100
200
300
400
500
Time (day)
0.00
0.52
2.0
5.6
16.
Power (W/m^2)^2

Fig. 9c

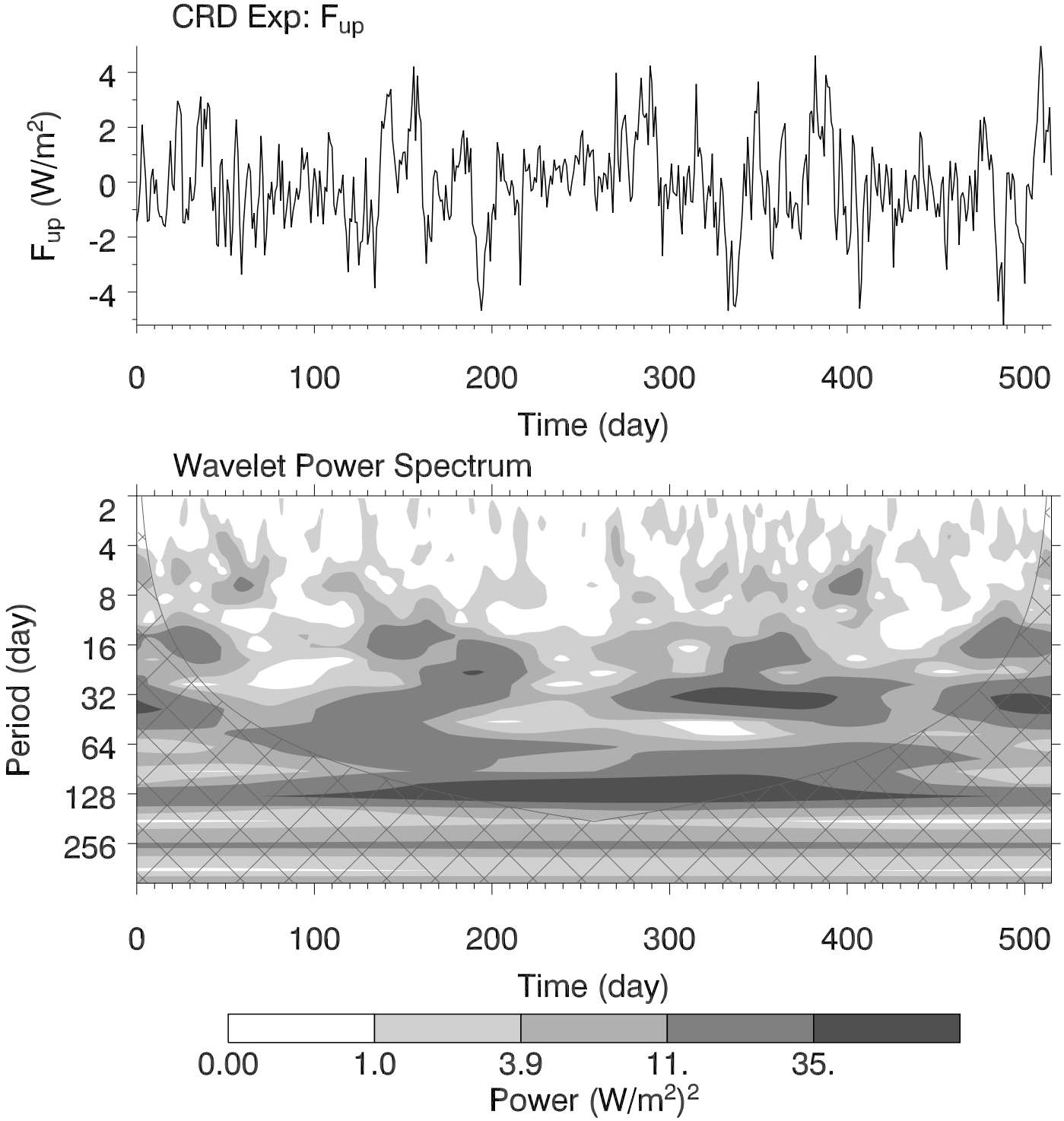
CRD Exp: F_{up}
F_{up} (W/m^2)
4
2
0
-2
-4
0
100
200
300
400
500
Time (day)
Wavelet Power Spectrum
Period (day)
2
4
8
16
32
64
128
256
0
100
200
300
400
500
Time (day)
0.00
1.0
3.9
11.
35.
Power (W/m^2)^2

Fig. 9d

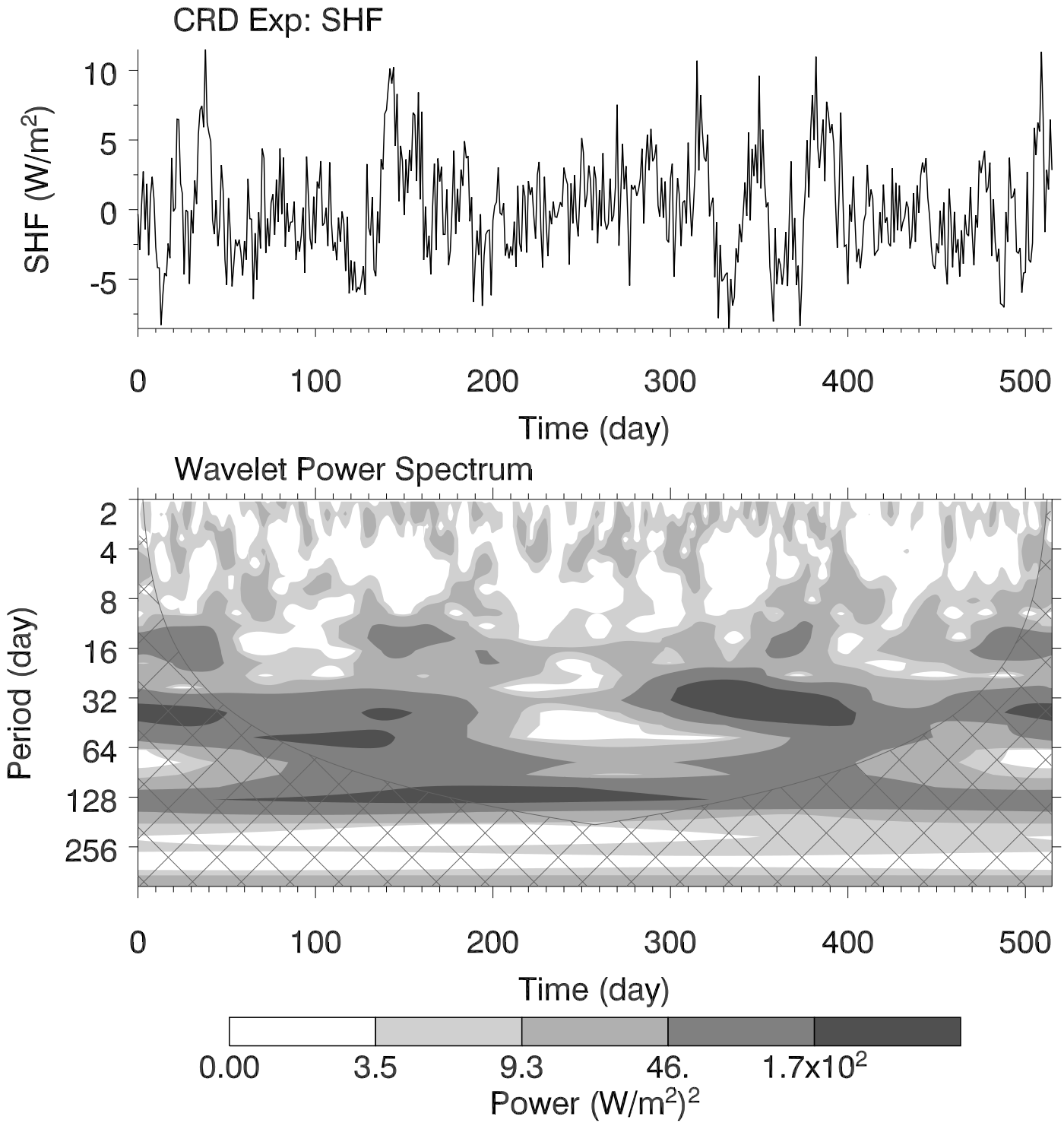
CRD Exp: SHF
SHF (W/m2)
10
5
0
-5
0
100
200
300
400
500
Time (day)
Wavelet Power Spectrum
Period (day)
2
4
8
16
32
64
128
256
0
100
200
300
400
500
Time (day)
0.00
3.5
9.3
46.
1.7x10^2
Power (W/m2)2

Fig. 9e

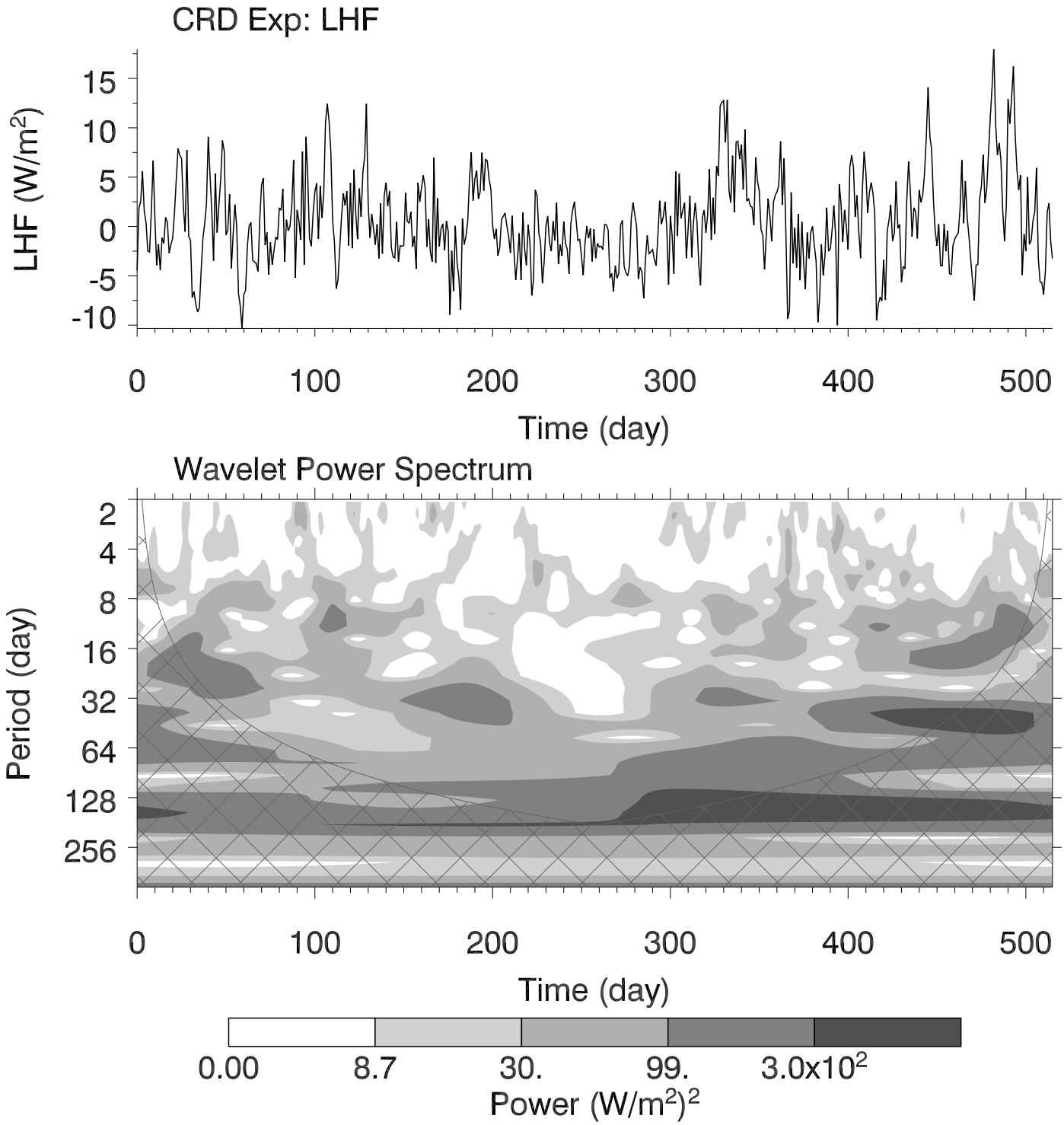
CRD Exp: LHF
LHF (W/m2)
15
10
5
0
-5
-10
0
100
200
300
400
500
Time (day)
Wavelet Power Spectrum
Period (day)
2
4
8
16
32
64
128
256
0
100
200
300
400
500
Time (day)
0.00
8.7
30.
99.
3.0x10^2
Power (W/m2)2

Fig. 9f

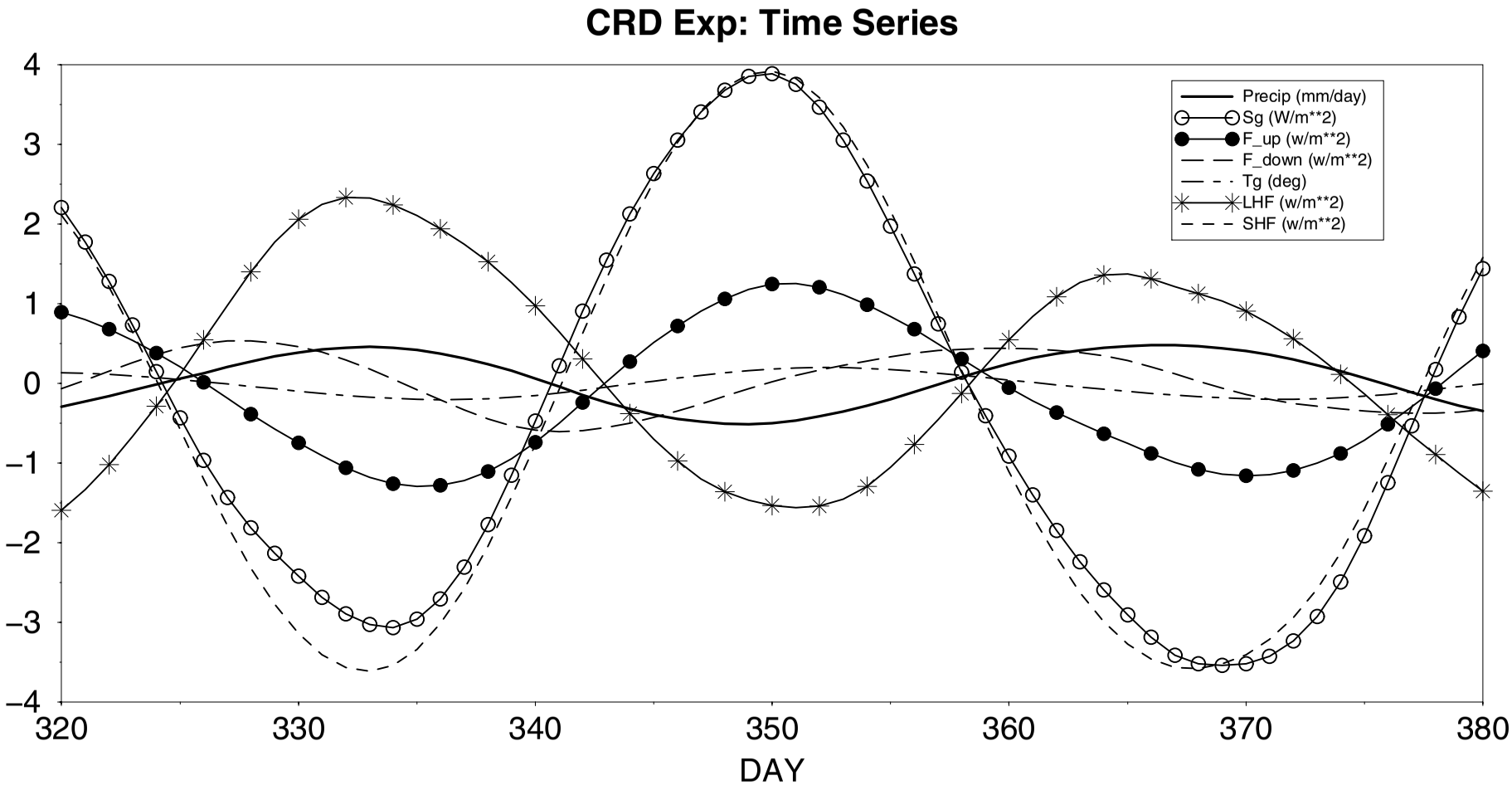
CRD Exp: Time Series
Precip (mm/day)
Sg (W/m**2)
F_up (w/m**2)
F_down (w/m**2)
Tg (deg)
LHF (w/m**2)
SHF (w/m**2)
4
3
2
1
0
−1
−2
−3
−4
320
330
340
350
360
370
380
DAY

Fig. 10